Rotational test spaces for a fully-implicit FVM and FEM for the DNS of fluid-particle interaction

Susanne Höllbacher [a,b,*], Gabriel Wittum [a,b]

[a] *King Abdullah University of Science and Technology (KAUST), Applied Mathematics and Computational Science (AMCS), Computer, Electrical and Mathematical Sciences and Engineering (CEMSE), Thuwal 23955-6900, Saudi Arabia*
[b] *Goethe-Center for Scientific Computing (G-CSC), Johann Wolfgang Goethe University, Kettenhofweg 139, 60325 Frankfurt, Germany*

ARTICLE INFO

ABSTRACT

The paper presents a fully-implicit and stable finite element and finite volume scheme for the simulation of freely moving particles in a fluid. The developed method is based on the Petrov-Galerkin formulation of a vertex-centered finite volume method (PG-FVM) on unstructured grids. Appropriate extension of the ansatz and test spaces lead to a formulation comparable to a fictitious domain formulation. The purpose of this work is to introduce a new concept of numerical modeling reducing the mathematical overhead which many other methods require. It exploits the identification of the PG-FVM with a corresponding finite element bilinear form. The surface integrals of the finite volume scheme enable a natural incorporation of the interface forces purely based on the original bilinear operator for the fluid. As a result, there is no need to expand the system of equations to a saddle-point problem. Like for fictitious domain methods the extended scheme treats the particles as rigid parts of the fluid. The distinguishing feature compared to most existing fictitious domain methods is that there is no need for an additional Lagrange multiplier or other artificial external forces for the fluid-solid coupling. Consequently, only one single solve for the derived linear system for the fluid together with the particles is necessary and the proposed method does not require any fractional time stepping scheme to balance the interaction forces between fluid and particles. For the linear Stokes problem we will prove the stability of both schemes. Moreover, for the stationary case the conservation of mass and momentum is not violated by the extended scheme, i.e. conservativity is accomplished within the range of the underlying, unconstrained discretization scheme. The scheme is applicable for problems in two and three dimensions.

© 2019 The Authors. Published by Elsevier Inc. This is an open access article under the CC BY-NC-ND license (http://creativecommons.org/licenses/by-nc-nd/4.0/).

1. Introduction

Many applications in engineering technology need to deal with the problem of describing the dynamics of many rigid particles within a fluid. In recent years problems from the field of biology and neuroscience account for the need of resolving single entities within cells. Surrounded by the highly viscous cytosol they displace a noticeable mass of fluid and far-field

---

interaction via the fluid is a relevant mechanism within the biological system. So called *direct numerical simulation* (DNS) is necessary to account for those effects.

Solving particulate fluid dynamics with DNS is a non-trivial task, because the particles move in time with the flow. DNS methods can be classified by two different approaches with respect to the handling of the grid: the class of boundary-fitted (moving grid) methods and non-boundary-fitted (fixed grid) methods. The first class, often denoted as *Arbitrary Lagrangian-Eulerian* (ALE) methods, employs conforming discretizations of the Navier-Stokes equations by remeshing the fluid domain and projecting the flow fields on the updated mesh at every time step. In case of large displacements, the remeshing of the grid is computationally very expensive. Moreover you need to deal with badly conditioned grids. We shall mention the contributions of Johnson and Tezduyar [20] and Hu and co-workers [18], [11], [12]. In the context of so called *front-tracking* methods, where the interface mesh is reconstructed at each time step, we want to mention the work of Unverdi and Tryggvason [41].

Fixed-grid methods eliminate the need for remeshing the domain by computing the solution on the original Eulerian grid. This class of methods shares the methodology that the spatial discretization of the fluid and solid belong to the same grid whose points do not conform with the interface. They are mainly differing in the strategy how to add the body force into the discrete equations. There are many different classes and categorizations of fixed-grid methods. We shall distinguish between the class of Distributed Lagrange Multiplier/Fictitious Domain (DLM/FDM) and the class of Immersed Boundary (IBM) methods.

In the DLM/FD method described by Glowinski et al. [14,15] the body force is introduced by extension of the fluid into the domain occupied by the particle. The forcing terms are therefore derived from the operator of the Navier-Stokes equations. This leads to a Lagrange multiplier field (LM) in the particle domain. The introduction of additional constraining equations for the LM leads to a doubling of degrees of freedom in the extended domain and a saddle-point problem needs to be solved. In order to avoid the solution of the saddle-point problem, Patankar and co-workers derived non-Lagrange multiplier versions of the original DLM/FD, [28], [27], [35]. The additional equations for the LM are replaced by a projection step, such that the total linear and angular momenta in the individual particle domain should be conserved [27]. Similar approaches are pursued by Veeramani et al. [42], Apte et al. [2], Blasco et al. [5]. Another non-Lagrange multiplier method was developed by Yu and Shao [52], in which an explicit expression for the particle velocities is derived by means of the primitive governing equations (Newton-Euler) for the motion of a particle. A further non-LM approach is the subspace projection method by Prignitz and Bänsch [31]. The discrete scheme possesses similarities to the one derived in this work. The DLM/FD of Wachs [44] relies on the original FD of Glowinski et al. [14] applying the weak formulation of the boundary condition and denotes the resulting saddle-point problem *combined momentum equations*. In the context of fictitious domain approaches we shall mention the fictitious boundary (FBM) method introduced by [48], where the stresses on the fluid-solid interface are integrated on a fictitious boundary.

Most fictitious domain methods introduce the body force in the whole domain of the particle and compute them implicitly (*weak forcing*) by means of a weak formulation. In contrast, the class of IBM employs explicit expressions for the body force (*direct forcing*). A good overview is given in [23]. The immersed boundary is represented by Lagrangian points on the interface and the body force is computed explicitly from the boundary condition which is defined at the Lagrangian points. By properly chosen discretized delta functions (DDF) the solution between the Eulerian and Lagrangian grid is linked. This approach was first described by Peskin [29] for Cartesian grids and a review can be found in [30]. The suitable design of the DDF is crucial for the stability and efficiency of the method. So called *regularized* DDF provide a stabilized scheme and lead to a smoothing of the interface. In the finite difference approach of Fadlun et al. [10] the boundary conditions are interpolated exactly. The well known drawback of such approaches aiming at a sharp interface implementation are discontinuities in the momentum forcing as the interface moves in time and space. Spurious oscillations of the forces are observed in many immersed boundary methods when the interface moves across the grid, [50]. The sharp-interface approach of Krause and Kummer [21] applies a *hierarchical moment fitting* strategy in combination with an extended discontinuous Galerkin discretization to overcome this problem. In [16] a sharp interface method is validated with respect to the numerical errors due to spurious pressure oscillations near the moving interface. The combination of conservation of mass and representation of a sharp interface was met by many following IBM. Uhlmann [39] and Uhlmann and Dušek [40] proposed a combination of direct forcing strategy and suitable DDF to smoothly transfer information between Eulerian and Lagrangian positions. Tschisgale et al. [38], Breugem [6] and Yang and Stern [50] derived similar approaches in order to suppress the oscillations due to the fixed grid.

A related source of numerical instability and spurious oscillations is the employment of a partitioned procedure for the numerical solution of the global formulation. In a partitioned approach, so called *explicit coupling* or *weak coupling*, the fluid and solid problems are solved separately. Iteration within each time step can eliminate numerical instabilities and provides a *strong coupling* strategy. Since most immersed boundary methods and also the referred fictitious domain methods decouple the solving procedure they need to implement a stable fractional time stepping scheme. In the partitioned approach of Burman and Fernandez [7] an additional interface time penalization term is introduced which acts to stabilize the pressure. Non-iterative immersed boundary methods were proposed by Tschisgale et al. [38] who derives a *semi-implicit* fluid-solid coupling scheme and also by Yang and Stern [50].

We finally want to mention the class of *phase-field* or *diffuse-interface* methods, cf. [33], [9], [36], [37], which are usually applied to evolving interfaces with surfactants, see also [1] for a review. In a diffuse-interface model the diffusion-advection equation for the interface is solved on a layer of finite thickness which contains the interface. The definition of so called

surface delta functions δ_Γ lead to a smoothed formulation for the interface forces comparable to those employed by the immersed boundary approaches of Uhlmann [39], Uhlmann and Dušek [40] or Tschisgale et al. [38].

The proposed method is comparable to a fictitious domain approach which extends the equations for the fluid on the domain occupied by the particle. It shall be applied to biological systems where only a few particles are interacting and a good approximation of the interaction is important. The central aim of this work is to introduce a new modeling approach which derives a system of equations based on the original operators without introducing additional mathematical overhead. This finally enables the development of a monolithic scheme which is easy to implement and solvable without operator splitting. Therefore, our focus will not be high efficiency for many-particle systems. Moreover, the manuscript is only the first step of a comprehensive novel approach to fluid-particle interaction. Topics like computational efficiency and parallelization will not be content of this paper.

We will also contrast our modeling approach with the DLM/FD of Glowinski et al. ([14], [15]) or Patankar et al. ([28], [27], [35]). The crucial ingredient of our approach is a Petrov-Galerkin formulation of a vertex-centered finite volume method (PG-FVM) and the exploitation of its well known identification with the linear finite element method. The according asymmetric bilinear form of the PG-FVM provides discrete spaces for the functions of the ansatz and the test space. We will derive the fluid-solid-coupling forces directly from the weak formulation by extending both, ansatz *and* test spaces. The distinguishing feature in comparison with the described DLM/FD of Glowinski et al. ([14], [15]) or Patankar et al. ([28], [27], [35]) is the inclusion of the rigid-body-motion (RBM) constraint directly into the definition of the extended spaces. No introduction of additional Lagrange multiplier is necessary which yields a system without saddle-point structure. Due to the surface integration provided by the finite volume formulation, the extended system naturally inherits the governing equations for the motion of a particle. As a consequence, the particle domain in our approach is *not* a fictitious domain. The additional functions for the extension of the spaces can rather be interpreted as certain DDF with degrees of freedom near the immersed interface which puts our approach near to an IBM. The resulting formulation is a fully-implicit immersed boundary scheme whose fluid and particle parts of the solution can be solved all together within one single step. For stationary problems the conservation of mass and momentum is inherited from the according conservative properties of the scheme for the bulk equations.

Finally, by identification with an analogous finite element scheme the following three derivations can be made: First, we can easily write down a finite element scheme for the DNS of particulate flow. Second, for the stationary, linear Stokes equations, stability can be proven for both schemes by application of standard finite element theory. And third, the resulting finite element scheme can be interpreted as diffuse-interface scheme with thickened interface and the extended finite element space can be interpreted as suitable DDF.

Due to the unfitted treatment of the interface spurious oscillations in the pressure are observed. To cope with those, we need a special treatment of the interface, which will be the topic of a separate publication.

The outline of this paper is as follows: After introducing the general continuous formulation of the model problem in Section 2, the discrete scheme for any presumed finite volume method will be derived in Section 3. Section 4 presents the particular example of a *vertex-centered* finite volume scheme. Based on that, a finite element method for particulate flow is presented at the end of Section 4. In Section 5 the stability and approximation properties for the linear Stokes problem will be proven. Finally, Section 6 presents numerical results.

2. Mathematical formulation

2.1. Governing equations

Let $\Omega \subset \mathbb{R}^d$, with $d = 2$, 3, be a polyhedral domain. For simplification of the notation we will take only one particle $P \subset \Omega$ into consideration and presume it to have a spherical shape. All derivations can be applied to each further particle. The domain occupied by the fluid will be denoted by $\Omega_f := \Omega \setminus P$, see Fig. 1. We assume an incompressible and Newtonian fluid and therefore the equations that govern the motion are the Navier-Stokes equations in Ω_f:

$$\rho_f \left(\frac{\partial}{\partial t} \mathbf{u} + \mathbf{u} \cdot \nabla \mathbf{u} \right) = \nabla \cdot \boldsymbol{\sigma} + \mathbf{g} \qquad \text{in } \Omega_f, \tag{1}$$

$$\nabla \cdot \mathbf{u} = 0 \qquad \text{in } \Omega_f, \tag{2}$$

$$\mathbf{u} = \mathbf{U} + \boldsymbol{\omega} \times \mathbf{r}(\vec{x}) \qquad \text{on } \partial P, \tag{3}$$

with stress tensor $\boldsymbol{\sigma} := -p\,\mathbf{I} + \mu_f(\nabla \mathbf{u} + \nabla \mathbf{u}^T)$, viscosity μ_f and density ρ_f of the fluid. We will presume constant fluid density. As already anticipated by the notation the volume force $\mathbf{g}$ will only be exerted by gravitation in all considered problems.

The particles arise as a boundary condition (3) in the equations of the fluid. Since their motion is assumed to be rigid, their velocity is composed accordingly by a translational component $\mathbf{U} \in \mathbb{R}^d$ and angular component $\boldsymbol{\omega} \in \mathbb{R}^d$. The motion can be described by the Newton-Euler equations and therefore $\mathbf{U}$ and $\boldsymbol{\omega}$ obey the relation

$$M_P \frac{d}{dt} \mathbf{U} = \mathbf{F}_H + M_P\,\mathbf{g}, \qquad I_P \frac{d}{dt} \boldsymbol{\omega} = \mathbf{T}_H, \tag{4}$$
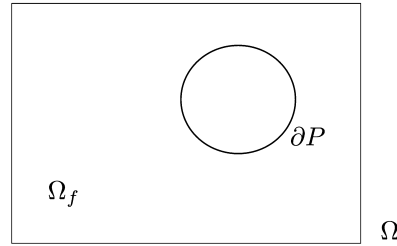
Fig. 1. Computational domain for the particulate flow problem comprising one embedded particle P.

with $\mathbf{F}_H$ and $\mathbf{T}_H$ being the hydrodynamic force and torque

$$\mathbf{F}_H = \int\limits_{\partial P} \boldsymbol{\sigma}(\vec{x})\,\mathbf{n}\,d\mathbf{s}, \qquad \mathbf{T}_H = \int\limits_{\partial P} \mathbf{r}(\vec{x}) \times \boldsymbol{\sigma}(\vec{x})\,\mathbf{n}\,d\mathbf{s}, \tag{5}$$

acting on the center of mass of the particle.

Remark 1 *(Full stress tensor).* It should be emphasized that the viscous terms in (4) and (5) depend on the complete stresses. As a consequence, the viscous dissipation in (1) for the fluid in the proximity of a particle equally needs to be modeled by the complete stress tensor rather than by the more common term $\nabla \mathbf{u}$, see also [14].

This paper is dedicated to developing a finite element and finite volume method for the simulation of particulate flow. For the latter case, we want to reconsider the underlying balance laws for fluid motion from which (1) and (2) are derived. Let $\mathcal{B}_h := \{B_i\}_{i=1}^N$ be a partition of the fluid domain Ω_f. A finite volume method for an incompressible fluid is required to satisfy the two balance laws

$$\int\limits_{B_i} \frac{d}{dt}\,\rho\,\mathbf{u}\,d\mathbf{x} = \int\limits_{\partial B_i} \boldsymbol{\sigma}\,\mathbf{n}\,d\mathbf{s} + \int\limits_{B_i} \mathbf{g}\,d\mathbf{x}, \tag{6}$$

$$\int\limits_{\partial B_i} \mathbf{u} \cdot \mathbf{n}\,d\mathbf{s} = 0, \tag{7}$$

for the momentum and mass on each so called *control volume* $B_i \subset \mathcal{B}_h$. Replacement of the total derivative $\frac{d}{dt}$ in (6) by the partial derivative in time $\frac{\delta}{\delta t}$ and the convective derivative $\mathbf{u} \cdot \nabla$ yields the non-linear term arising in the usual form of the Navier-Stokes equations. In order to avoid unmanageably long expressions we will keep utilizing the total derivative also for the formulation of the bilinear forms derived in the following section.

2.2. Two different bilinear forms describing the motion of a fluid

With the function space of piecewise constants on each $B_i \in \mathcal{B}_h$ defined as

$$\mathcal{Q}_h := \{v(\vec{x}) \in L^2(\Omega) \,:\, v(\vec{x})|_{B_i} = \text{const}, \; B_i \in \mathcal{B}_h\}$$

and $\mathcal{V}_h := [\mathcal{Q}_h]^d$ a *virtual* second argument can be introduced into the integrals in (6) and (7). The bilinear forms $a_{\text{FV}}(\mathbf{u}, \mathbf{v}) : \mathbf{H}_0^1(\Omega) \times \mathcal{V}_h \to \mathbb{R}$ and $b_{\text{FV}}(\mathbf{v}, p) : \mathcal{V}_h \times L_0^2(\Omega) \to \mathbb{R}$ for velocity and pressure can therefore be derived directly from the balance equations as

$$a_{\text{FV}}(\mathbf{u}, \mathbf{v}) := \sum_{i=1}^N \left(\rho \int\limits_{B_i} \frac{d}{dt}\,\mathbf{u} \cdot \mathbf{v}\,d\mathbf{x} - \int\limits_{\partial B_i} \mu(\nabla \mathbf{u} + \nabla \mathbf{u}^T)\,\mathbf{n} \cdot \mathbf{v}\,d\mathbf{s} \right), \tag{8}$$

$$b_{\text{FV}}(\mathbf{v}, p) := \sum_{i=1}^N \int\limits_{\partial B_i} p\,\mathbf{n} \cdot \mathbf{v}\,d\mathbf{s}, \tag{9}$$

with the usual Lebesgue and Sobolev spaces $L_0^2(\Omega)$ and $\mathbf{H}_0^1(\Omega)$. Since the ansatz space $\mathbf{H}_0^1(\Omega)$ differs from the test space $\mathcal{V}_h$, a finite volume method is often interpreted as a Petrov-Galerkin method based on an appropriate bilinear form. We introduce the notation $\overline{b}_{\text{FV}}(\mathbf{u}, q) : \mathbf{H}_0^1(\Omega) \times \mathcal{Q}_h \to \mathbb{R}$ for the according bilinear form of equation (7) since it comprises the same operation as the bilinear form $b_{\text{FV}}(\cdot, \cdot)$, but maps the space $\mathbf{H}_0^1(\Omega) \times \mathcal{Q}_h$ onto $\mathbb{R}$. The collection of the linear functionals

in (6), (7) gets transformed into bilinear forms and the corresponding finite volume method reads: Find $\mathbf{u} \in \mathbf{H}_0^1(\Omega)$, $p \in L_0^2(\Omega)$ s.t.

$$a_{\text{FV}}(\mathbf{u}, \mathbf{v}) + b_{\text{FV}}(\mathbf{v}, p) = (\mathbf{g}, \mathbf{v}) \qquad \forall \mathbf{v} \in \mathcal{V}_h, \tag{10}$$

$$\overline{b}_{\text{FV}}(\mathbf{u}, q) = 0 \qquad \forall q \in \mathcal{Q}_h, \tag{11}$$

with the L^2-scalar product

$$(\mathbf{g}, \mathbf{v}) := \int\limits_{\Omega} \mathbf{g} \cdot \mathbf{v} \, d\mathbf{x}.$$

For the derivation of a FEM for particulate flow we will define the according operators of a finite element method. In contrast to a FVM the bilinear forms are derived from the weak formulation of the system of PDE (1) - (3). Applying partial integration to the related variational formulation we get the well known operators $a_{\text{FE}} : \mathbf{H}_0^1(\Omega) \times \mathbf{H}_0^1(\Omega) \to \mathbb{R}$ and $b_{\text{FE}} : L_0^2(\Omega) \times \mathbf{H}_0^1(\Omega) \to \mathbb{R}$ defined as

$$a_{\text{FE}}(\mathbf{u}, \mathbf{v}) := \rho \int\limits_{\Omega} \frac{d}{dt} \mathbf{u} \cdot \mathbf{v} \, d\mathbf{x} + \int\limits_{\Omega} 2\,\mu\, \mathbf{D}[\mathbf{u}] : \mathbf{D}[\mathbf{v}] \, d\mathbf{x}, \tag{12}$$

$$b_{\text{FE}}(\mathbf{v}, p) := - \int\limits_{\Omega} p \, \nabla \cdot \mathbf{v} \, d\mathbf{x}, \tag{13}$$

with the *rate-of-strain* tensor $\mathbf{D}[\mathbf{u}] := 0.5\,(\nabla \mathbf{u} + \nabla \mathbf{u}^T)$. Due to Remark 1 the weak formulation involves $\mathbf{D}[\mathbf{u}] : \mathbf{D}[\mathbf{v}]$ instead of the more usual term $\nabla \mathbf{u} : \nabla \mathbf{v}$. The corresponding weak formulation of (1) - (3) reads: Find $\mathbf{u} \in \mathbf{H}_0^1(\Omega)$, $p \in L_0^2(\Omega)$ s.t.

$$a_{\text{FE}}(\mathbf{u}, \mathbf{v}) + b_{\text{FE}}(\mathbf{v}, p) = (\mathbf{g}, \mathbf{v}) \qquad \forall \mathbf{v} \in \mathbf{H}_0^1(\Omega), \tag{14}$$

$$b_{\text{FE}}(\mathbf{u}, q) = 0 \qquad \forall q \in L_0^2(\Omega). \tag{15}$$

Remark 2. The bilinear form $a_{\text{FV}}(\cdot, \cdot)$ can be derived with more mathematical rigor from a so called *generalized variational form*, which is described for example in [4] for the convection-diffusion equation. That enables the theoretical analysis of convergence properties of a finite volume solution. For the purposes of this paper we abandon that approach via a variational formulation. Instead, we simply argue that the given integral equations (6) and (7) can be written as a bilinear form. At the end of that section we will see how we can profit from the introduction of a second argument for the derivation of a stable scheme.

2.3. Extension of the spaces: introducing a rotational test space

We can describe the common ansatz space for the fluid and the particle on $\Omega := \Omega_f \cup P$ by

$$\mathcal{U}^{\text{RBM}} := \{(\mathbf{u}, \mathbf{U}, \boldsymbol{\omega}) : \mathbf{u} \in \mathbf{H}_0^1(\Omega),$$
$$\mathbf{u}(\vec{x})|_P = \mathbf{U} + \boldsymbol{\omega} \times \mathbf{r}(\vec{x}), \ \mathbf{U}, \ \boldsymbol{\omega} \in \mathbb{R}^d,$$
$$\mathbf{r}(\vec{x}) := \vec{x} - \vec{x}_c\}$$

with center of mass $\vec{x}_c$ of P. With characteristic function $\chi_P(\vec{x})|_P \equiv 1$, $\chi_P(\vec{x}) = 0$ else, and the radial vector $\mathbf{r}(\vec{x}) := \vec{x} - \vec{x}_c$ the distinguished spaces

$$\mathcal{U}^f := \mathbf{H}_0^1(\Omega_f), \qquad \mathcal{U}^{\text{lin}} := \{\mathbf{U}\,\chi_P(\vec{x}), \ \mathbf{U} \in \mathbb{R}^d\}, \quad \mathcal{U}^{\text{rot}} := \{[\,\boldsymbol{\omega} \times \mathbf{r}(\vec{x})\,]\,\chi_P(\vec{x}), \ \boldsymbol{\omega} \in \mathbb{R}^d\}$$

provide the representation of $\mathcal{U}^{\text{RBM}}$ as the combined space

$$\mathcal{U}^{\text{RBM}} = \mathcal{U}^f + \mathcal{U}^{\text{lin}} + \mathcal{U}^{\text{rot}}.$$

The set of vectors $\{\mathbf{e}_k\}_{k=1}^d$ and $\{\mathbf{e}_k \times \mathbf{r}(\vec{x})\}_{k=1}^d$ form a basis of $\mathcal{U}^{\text{lin}}$ and $\mathcal{U}^{\text{rot}}$, respectively.

For a rigid body no pressure field can be reasonably defined in P. Moreover, pressure inside P is not relevant for the dynamics of the coupled system. We therefore define the ansatz space for the pressure only on the domain Ω_f as

$$\mathcal{P}^{\text{RBM}} = L_0^2(\Omega_f) := \{p \in L^2(\Omega_f) \ : \int\limits_{\Omega_f} p \, d\mathbf{x} = 0\}. \tag{16}$$

We want to emphasize that many discretizations for particulate flow employing a fictitious domain approach like [14], [27], [35], [2], [5] compute a fictitious pressure field within the particle. For the method developed in this work no pressure will be computed in P.

With regard to the next remark it should be emphasized that the equations for a homogeneous fluid usually do not contain the conservation of angular momentum. First of all, due to the symmetry of the stress tensor $\boldsymbol{\sigma}$ the conservation of angular momentum already follows from the conservation of linear momentum. Furthermore, in the limit of a continuous fluid a single point cannot possess a rotational component. In case of a particle with finite size, however, it can also rotate. This gets reflected in the supply of degrees of freedom, as stated in the following remark:

Remark 3 (*Independent rotational component*). The vectors $\{\mathbf{e}_k, \mathbf{e}_k \times \mathbf{r}(\vec{x})\}_{k=1}^d$ are *pointwise* dependent, i.e. for each $\vec{x} \in P$ the vectors $\{\mathbf{e}_k, \mathbf{e}_k \times \mathbf{r}(\vec{x})\}_{k=1}^d$ are linearly dependent. In contrast, the vectors $\{\mathbf{e}_k, \mathbf{e}_k \times \mathbf{r}(\vec{x})\}_{k=1}^d$ are *locally* independent, i.e. for each open domain $M \subset P$ and $\mathbf{u}_1(\vec{x}) := \mathbf{U}_1 + \boldsymbol{\omega}_1 \times \mathbf{r}(\vec{x})$, $\mathbf{u}_2(\vec{x}) := \mathbf{U}_2 + \boldsymbol{\omega}_2 \times \mathbf{r}(\vec{x})$, $\vec{x} \in M$ and $\mathbf{U}_1, \mathbf{U}_2, \boldsymbol{\omega}_1, \boldsymbol{\omega}_2 \in \mathbb{R}^d$ it is:

$$\mathbf{u}_1(\vec{x}) = \mathbf{u}_2(\vec{x}) \text{ for all } \vec{x} \in M \iff \mathbf{U}_1 = \mathbf{U}_2 \text{ and } \boldsymbol{\omega}_1 = \boldsymbol{\omega}_2. \tag{17}$$

Proof. The pointwise dependence is clear. Equally the conclusion '$\Longleftarrow$' in (17) directly follows. Let us assume $\mathbf{u}_1(\vec{x}) = \mathbf{u}_2(\vec{x})$ and $\boldsymbol{\omega}_1 \neq \boldsymbol{\omega}_2$. We define $\overline{\mathbf{U}} := \mathbf{U}_1 - \mathbf{U}_2$, $\overline{\boldsymbol{\omega}} := \boldsymbol{\omega}_1 - \boldsymbol{\omega}_2$ and $\overline{\mathbf{u}}(\vec{x}) := \mathbf{u}_1(\vec{x}) - \mathbf{u}_2(\vec{x}) = \overline{\mathbf{U}} + \overline{\boldsymbol{\omega}} \times \mathbf{r}(\vec{x})$. Because of $\mathbf{u}_1(\vec{x}) = \mathbf{u}_2(\vec{x})$ it is

$$\overline{\mathbf{U}} = -\overline{\boldsymbol{\omega}} \times \mathbf{r}(\vec{x}) \text{ for all } \vec{x} \in M. \tag{18}$$

Subtracting equation (18) for two different $\vec{x}_1, \vec{x}_2 \in M$ gives $\overline{\boldsymbol{\omega}} \times [\mathbf{r}(\vec{x}_1) - \mathbf{r}(\vec{x}_2)] = 0$ and since $\mathbf{r}(\vec{x}_1) \neq \mathbf{r}(\vec{x}_2)$ it follows $\overline{\boldsymbol{\omega}} = \mathbf{0}$ or $\overline{\boldsymbol{\omega}} = \lambda [\mathbf{r}(\vec{x}_1) - \mathbf{r}(\vec{x}_2)]$ with $\lambda \neq 0$. Since by construction the vectors $\boldsymbol{\omega}_1$ and $\boldsymbol{\omega}_2$ point in orthogonal direction to the rotating plane described by $\mathbf{r}(\vec{x}_1)$ and $\mathbf{r}(\vec{x}_2)$, the latter case can be excluded. $\square$

According to Remark 3 the product space $\mathcal{U}^{\text{RBM}}$ even forms a *direct* sum, i.e.

$$\mathcal{U}^{\text{RBM}} = \mathcal{U}^f \oplus \mathcal{U}^{\text{lin}} \oplus \mathcal{U}^{\text{rot}}. \tag{19}$$

Remark 4 (*Regularity*). We want to emphasize that the independence of the spaces $\mathcal{U}^f$, $\mathcal{U}^{\text{lin}}$ and $\mathcal{U}^{\text{rot}}$ is a necessary condition for the regularity of a discrete scheme, since that will be derived from the direct sum of the discrete basis of each space.

In analogy to the definition of the ansatz space $\mathcal{U}^{\text{RBM}}$ we can enrich the test spaces of the two bilinear forms defined in Section 2.2 with the same reservoir of degrees of freedom. For this purpose, let $\mathcal{B}_h^f$ be a partition of Ω_f. Then $\mathcal{B}_h := \{\mathcal{B}_h^f \cup P\}$ forms a partition of Ω and $\mathcal{Q}_h^f$, $\mathcal{V}_h^f$ can be defined in analogy to $\mathcal{Q}_h$ and $\mathcal{V}_h$ with respect to Ω_f. Setting $\mathcal{V}^{\text{lin}} := \mathcal{U}^{\text{lin}}$ and $\mathcal{V}^{\text{rot}} := \mathcal{U}^{\text{rot}}$ the test space for the operator $a_{\text{FV}}(\cdot, \cdot)$ reads

$$\mathcal{V}^{\text{RBM}} := \mathcal{V}_h^f \oplus \mathcal{V}^{\text{lin}} \oplus \mathcal{V}^{\text{rot}}.$$

In accordance to the definition of the ansatz space for the pressure in (16) we define the test space by $\mathcal{Q}^{\text{RBM}} := \mathcal{Q}_h^f$ equally excluding the domain P.

For the bilinear forms $a_{\text{FE}}(\cdot, \cdot)$ and $b_{\text{FE}}(\cdot, \cdot)$ we choose the test spaces symmetrically to the ansatz space as $\mathcal{V}^{\text{RBM}} := \mathcal{U}^{\text{RBM}}$ and $\mathcal{Q}^{\text{RBM}} := \mathcal{P}^{\text{RBM}}$.

Remark 5. Since the space $\mathcal{Q}^{\text{RBM}}$ excludes the domain P the mass will not be balanced for the domain P. By means of

$$\nabla \cdot [\mathbf{U} + \boldsymbol{\omega} \times \mathbf{r}(\vec{x})] = \mathbf{r}(\vec{x}) \cdot \underbrace{(\nabla \times \boldsymbol{\omega})}_{=0} + \boldsymbol{\omega} \cdot \underbrace{(\nabla \times \mathbf{r}(\vec{x}))}_{=0} = 0$$

it is

$$0 = \int_P \nabla \cdot [\mathbf{U} + \boldsymbol{\omega} \times \mathbf{r}(\vec{x})] \, d\mathbf{x} = \int_{\partial P} [\mathbf{U} + \boldsymbol{\omega} \times \mathbf{r}(\vec{x})] \cdot \mathbf{n} \, d\mathbf{s}.$$

Thus, due to the rigid body motion of P, the conservation of mass within P is automatically satisfied.

For the derivation of the FVM and FEM for particulate flow we define the bilinear forms $A(\cdot, \cdot) := a_{\text{FV}}(\cdot, \cdot) + b_{\text{FV}}(\cdot, \cdot)$ and $A(\cdot, \cdot) := a_{\text{FE}}(\cdot, \cdot) + b_{\text{FE}}(\cdot, \cdot)$, respectively. On the correspondingly enriched spaces $\mathcal{U}^{\text{RBM}} \times \mathcal{P}^{\text{RBM}}$ the resulting system for the momentum equation finally reads:

Find $\mathbf{u} = \mathbf{u}_f + \mathbf{u}_{\text{lin}} + \mathbf{u}_{\text{rot}} \in \mathcal{U}^{\text{RBM}}$ and $p \in \mathcal{P}^{\text{RBM}}$ s.t.

$$A(\mathbf{u}_f, p\,; \mathbf{v}_f) + A(\mathbf{u}_{\text{lin}}, p\,; \mathbf{v}_f) + A(\mathbf{u}_{\text{rot}}, p\,; \mathbf{v}_f) = (\mathbf{g}, \mathbf{v}_f)\ \forall \mathbf{v}_f \in \mathcal{V}_h^f, \tag{20}$$

$$A(\mathbf{u}_f, p\,; \mathbf{v}_{\text{lin}}) + A(\mathbf{u}_{\text{lin}}, p\,; \mathbf{v}_{\text{lin}}) + A(\mathbf{u}_{\text{rot}}, p\,; \mathbf{v}_{\text{lin}}) = (\mathbf{g}, \mathbf{v}_{\text{lin}})\ \forall \mathbf{v}_{\text{lin}} \in \mathcal{V}^{\text{lin}}, \tag{21}$$

$$A(\mathbf{u}_f, p\,; \mathbf{v}_{\text{rot}}) + A(\mathbf{u}_{\text{lin}}, p\,; \mathbf{v}_{\text{rot}}) + A(\mathbf{u}_{\text{rot}}, p\,; \mathbf{v}_{\text{rot}}) = (\mathbf{g}, \mathbf{v}_{\text{rot}})\ \forall \mathbf{v}_{\text{rot}} \in \mathcal{V}^{\text{rot}}. \tag{22}$$

It should be emphasized that by means of the extension of the ansatz space two additive terms arise in system (20), that is $A(\mathbf{u}_{\text{lin}}, p\,; \mathbf{v}_f)$ and $A(\mathbf{u}_{\text{rot}}, p\,; \mathbf{v}_f)$. The extension of test space results in the two additional systems (21), (22).

2.4. Two bilinear forms on the extended spaces

In the sequel, we will specify equations (21) and (22) for the two bilinear forms of the FVM and FEM. The movement of the particle will be described in Lagrangian frame (cf. Section 3.1), i.e. the total derivative will be used for the derivation in time. Consequently, the non-linear terms will not arise explicitly in the equations. Starting with the FVM, i.e. $A(\cdot, \cdot) := a_{\text{FV}}(\cdot, \cdot) + b_{\text{FV}}(\cdot, \cdot)$, the additional equations (21), (22) are the original Newton-Euler equations (4) for the motion of a particle:

Lemma 1. Let $A(\cdot, \cdot) := a_{\text{FV}}(\cdot, \cdot) + b_{\text{FV}}(\cdot, \cdot)$. For $\boldsymbol{u} = \boldsymbol{u}_f + \boldsymbol{u}_{lin} + \boldsymbol{u}_{rot}$ with $\boldsymbol{u}_{lin} := \boldsymbol{U} \chi_P(\vec{x})$, $\boldsymbol{u}_{rot} := [\,\boldsymbol{\omega} \times \boldsymbol{r}(\vec{x})\,]\, \chi_P(\vec{x})$ and test functions $\boldsymbol{v}_{lin} := \boldsymbol{V} \chi_P(\vec{x})$ and $\boldsymbol{v}_{rot} := [\,\boldsymbol{\zeta} \times \boldsymbol{r}(\vec{x})\,]\, \chi_P(\vec{x})$ we get the following equivalent expressions:

$$A(\boldsymbol{u}, p\,; \boldsymbol{v}_{lin}) = (\boldsymbol{g}, \boldsymbol{v}_{lin}) \Longleftrightarrow M_P \frac{d}{dt}\, \boldsymbol{U} \cdot \boldsymbol{V} = \int_{\partial P} \boldsymbol{\sigma}(\vec{x})\, \boldsymbol{n} \cdot \boldsymbol{V}\, d\boldsymbol{s} + M_P\, \boldsymbol{g} \cdot \boldsymbol{V}, \tag{23}$$

$$A(\boldsymbol{u}, p\,; \boldsymbol{v}_{rot}) = (\boldsymbol{g}, \boldsymbol{v}_{rot}) \Longleftrightarrow I_P \frac{d}{dt}\, \boldsymbol{\omega} \cdot \boldsymbol{\zeta} = \int_{\partial P} \boldsymbol{r}(\vec{x}) \times \boldsymbol{\sigma}(\vec{x})\, \boldsymbol{n} \cdot \boldsymbol{\zeta}\, d\boldsymbol{s}. \tag{24}$$

Proof. With $a_{\text{FV}}(\cdot, \cdot)$ as in (8) and using $\mathbf{a} \cdot (\mathbf{b} \times \mathbf{r}) = (\mathbf{r} \times \mathbf{a}) \cdot \mathbf{b}$ with $\mathbf{a}, \mathbf{b}, \mathbf{r} \in \mathbb{R}^d$ we get

$$A(\mathbf{u}, p\,; \mathbf{v}_{\text{lin}}) = \rho_P \frac{d}{dt} \int_P \mathbf{u}(\vec{x}) \cdot \mathbf{V}\, d\mathbf{x} - \int_{\partial P} \boldsymbol{\sigma}(\vec{x})\, \mathbf{n} \cdot \mathbf{V}\, d\mathbf{s},$$

$$A(\mathbf{u}, p\,; \mathbf{v}_{\text{rot}}) = \rho_P \frac{d}{dt} \int_P \mathbf{r}(\vec{x}) \times \mathbf{u}(\vec{x}) \cdot \boldsymbol{\zeta}\, d\mathbf{x} - \int_{\partial P} \mathbf{r}(\vec{x}) \times \boldsymbol{\sigma}(\vec{x})\, \mathbf{n} \cdot \boldsymbol{\zeta}\, d\mathbf{s}.$$

Substituting $\mathbf{u}(\vec{x})|_P = \mathbf{U} + \boldsymbol{\omega} \times \mathbf{r}(\vec{x})$ yields

$$\rho_P \frac{d}{dt} \int_P [\mathbf{U} + \boldsymbol{\omega} \times \mathbf{r}(\vec{x})\,]\, d\mathbf{x} = \rho_P \frac{d}{dt} \int_P \mathbf{U}\, d\mathbf{x} + \rho_P \frac{d}{dt} \int_P \boldsymbol{\omega} \times \mathbf{r}(\vec{x})\, d\mathbf{x} = M_P \frac{d}{dt} \mathbf{U}.$$

With $\boldsymbol{\omega} = [\mathbf{r}(\vec{x}) \times \mathbf{u}(\vec{x})] / |\mathbf{r}(\vec{x})|^2$ and the special case of a spherical particle we have

$$\rho_P \frac{d}{dt} \int_P \mathbf{r}(\vec{x}) \times \mathbf{u}(\vec{x})\, d\mathbf{x} = \rho_P \frac{d}{dt} \int_P \boldsymbol{\omega} |\mathbf{r}(\vec{x})|^2\, d\mathbf{x} = I_P \frac{d}{dt} \boldsymbol{\omega}.$$

Finally, we get

$$(\mathbf{g}, \mathbf{v}_{\text{lin}}) = \rho_P \int_P \mathbf{g} \cdot \mathbf{V}\, d\mathbf{x} = M_P\, \mathbf{g} \cdot \mathbf{V} \ \text{ and } \ (\mathbf{g}, \mathbf{v}_{\text{rot}}) = \rho_P \int_P \mathbf{r}(\vec{x}) \times \mathbf{g} \cdot \boldsymbol{\zeta}\, d\mathbf{x} = 0. \quad \square$$

Regarding Lemma 1, the Newton-Euler equations (4) for a rigid body motion can therefore directly be derived from the bilinear form of the finite volume scheme with respect to the extended spaces. We end up with the following system (comprising 3 or 6 additional equations for the motion of the particle in 2 or 3 dimensions, respectively):

Find $\mathbf{u} = \mathbf{u}_f + \mathbf{U} + [\,\boldsymbol{\omega} \times \mathbf{r}\,] \in \mathcal{U}^{\text{RBM}}$, s.t.

$$a(\mathbf{u}_f, \mathbf{v}_f) + a(\mathbf{U}, \mathbf{v}_f) + a(\boldsymbol{\omega} \times \mathbf{r}, \mathbf{v}_f) = (\mathbf{g}, \mathbf{v}_f) \qquad \forall \mathbf{v}_f \in \mathcal{V}_h^f, \tag{25}$$

$$M_P \frac{d}{dt} \mathbf{U} \cdot \mathbf{V} - \int_{\partial P} \boldsymbol{\sigma}(\vec{x})\, \mathbf{n} \cdot \mathbf{V}\, d\mathbf{s} = M_P\, \mathbf{g} \cdot \mathbf{V} \quad \forall \mathbf{V} \in \mathbb{R}^d, \tag{26}$$

$$I_P \frac{d}{dt} \boldsymbol{\omega} \cdot \boldsymbol{\zeta} - \int_{\partial P} \mathbf{r}(\vec{x}) \times \boldsymbol{\sigma}(\vec{x})\, \mathbf{n} \cdot \boldsymbol{\zeta}\, d\mathbf{s} = 0 \qquad \forall \boldsymbol{\zeta} \in \mathbb{R}^d. \tag{27}$$

The essential step of the described approach is the symmetric extension and therefore projection of the test space: Testing with the functions of the spaces $\mathcal{V}^{\text{lin}}$ and $\mathcal{V}^{\text{rot}}$ is equivalent to generating the two systems (26) and (27) of equations for the domain P. The equivalence (24) precisely states that appending a rotational component to the test space leads to the equation for the conservation of angular momentum. We want to highlight that finding by the following Corollary:

Corollary 1 (Rotational test space – FV). *Testing the bilinear form of the finite volume formulation with the rotational basis leads to the equation for the conservation of angular momentum.*

With regard to the previous considerations we want to state the following interim conclusions:

Remark 6.

1. The symmetric extension of Ω_f to Ω by means of $\mathcal{U}^{\text{RBM}}$ and $\mathcal{V}^{\text{RBM}}$ leads to the system (25)–(27) of equations which does *not* possess the structure of a saddle-point problem. In more detail we can interpret the extensions of the test and ansatz spaces as follows:
   i. $\mathcal{V}_h^f \to \mathcal{V}^{\text{RBM}}$: The extension of the test space $\mathcal{V}_h^f$ to $\mathcal{V}^{\text{RBM}}$ generates the additional equations (26), (27) which serve as *constraining equations*. Instead of the common constraining Dirichlet condition of rigid body motion on the interface (3), the equations (26), (27) are naturally derived from the original governing equations.
   ii. $\mathcal{U}^f \to \mathcal{U}^{\text{RBM}}$: The extension of the ansatz space $\mathcal{U}^f$ to $\mathcal{U}^{\text{RBM}}$ generates additive terms to the Navier-Stokes equations for the fluid which can physically be interpreted as *external* forces. In particular, these are no artificial forces, but implicitly arise from the additional degrees of freedom assigned to the domain P.
2. Due to Remark 3 (or equivalently (19)) the resulting system (25) - (27) of equations is well posed. The additional equations (26) and (27) lead to a consistent and stable closing of the system including the additional degrees of freedom $\mathbf{U}$, $\boldsymbol{\omega} \in \mathbb{R}^d$.
3. The operator $\boldsymbol{\sigma}\,\mathbf{n}$ evaluated on ∂P comprises the gradient of the velocity field on the interface in normal direction pointing into Ω_f. Therefore, the integral not only depends on $\mathbf{U}$ and $\boldsymbol{\omega}$ but also on $\mathbf{u}_f$. Consequently, the resulting system is fully coupled.
4. The restriction of the velocity field in $P \subset \Omega$ to a rigid body motion corresponds to a projection of the solution. The interface condition (3) turns into a *conditioned ansatz space*. Besides, it does not have the role of a *fictitious* velocity field.
5. From a physical point of view it seems obvious to add the conservation of the angular momentum to the system of equations after adding a rotational component to the solution in P. Lemma 1 states that the angular momentum equation is equivalent to the extension of the test space by rotational basis functions. In Section 4 we will see that it is even equivalent to the variation with rotational test functions. The essential advantage of that equivalence is the possibility to prove stability, existence and unity of the solution.

By extending the test space the constraining equations for the new degrees of freedom of the extended ansatz space naturally arise from the original bilinear form. The result is an implicit incorporation of the immersed boundary condition (3) into the governing equations (6) and (7). Many discretizations, cf. [14], [39], utilize the original boundary condition (3) as conditioning equation. By enforcing that equation weakly via (28) and introducing the corresponding variables $\boldsymbol{\lambda}$ as Lagrange multiplier via (29) the system derived in [14] gets extended by

$$\langle \mathbf{u} - [\mathbf{U} + \boldsymbol{\omega} \times \mathbf{r}(\vec{x})], \boldsymbol{\mu} \rangle_P = 0, \tag{28}$$

$$\langle \boldsymbol{\lambda}, \mathbf{v} - [\mathbf{V} + \boldsymbol{\zeta} \times \mathbf{r}(\vec{x})] \rangle_P = 0. \tag{29}$$

In contrast to our approach the equations (28), (29) can not be naturally derived from the bulk equations. In the case of a FEM we want to hypothesize a possible reason, why (28), (29) are utilized in many schemes to model particulate flow: Because of the rigidity of P it is $\nabla\mathbf{u} + \nabla\mathbf{u}^T|_P = \mathbf{0}$, i.e. the velocity term of the stresses cancel. Let $A(\cdot, \cdot) := a_{\text{FE}}(\cdot, \cdot) + b_{\text{FE}}(\cdot, \cdot)$. We derive an analogous statement to Lemma 1:

Lemma 2. *Let $A(\cdot, \cdot) := a_{\text{FE}}(\cdot, \cdot) + b_{\text{FE}}(\cdot, \cdot)$. For $\boldsymbol{u} = \boldsymbol{u}_f + \boldsymbol{u}_{lin} + \boldsymbol{u}_{rot}$ with $\boldsymbol{u}_{lin} := \boldsymbol{U}\,\chi_P(\vec{x})$, $\boldsymbol{u}_{rot} := [\,\boldsymbol{\omega} \times \boldsymbol{r}(\vec{x})\,]\,\chi_P(\vec{x})$ and test functions $\boldsymbol{v}_{lin} := \boldsymbol{V}\,\chi_P(\vec{x})$ and $\boldsymbol{v}_{rot} := [\,\boldsymbol{\zeta} \times \boldsymbol{r}(\vec{x})\,]\,\chi_P(\vec{x})$ we get the following equivalent expressions:*

$$A(\boldsymbol{u}, p\,; \boldsymbol{v}_{lin}) = (\boldsymbol{g}, \boldsymbol{v}_{lin}) \Longleftrightarrow M_P \frac{d}{dt}\boldsymbol{U} \cdot \boldsymbol{V} = M_P\,\boldsymbol{g} \cdot \boldsymbol{V}, \tag{30}$$

$$A(\boldsymbol{u}, p\,; \boldsymbol{v}_{rot}) = (\boldsymbol{g}, \boldsymbol{v}_{rot}) \Longleftrightarrow I_P \frac{d}{dt}\boldsymbol{\omega} \cdot \boldsymbol{\zeta} = 0. \tag{31}$$

Proof. For the time dependent term and the force term the argumentation is equivalent to the one in the proof of Lemma 1. Because of $\nabla\mathbf{u} + \nabla\mathbf{u}^T|_P = \mathbf{0}$ and since pressure does not account for the movement in P the stress term is eliminated. The remaining terms are those in (30) and (31). $\square$

By means of Lemma 2 an analogous result as in Corollary 1 can not be derived for the variational formulation (14), (15). We want to oppose the following statement to Corollary 1:

Corollary 2 *(Rotational test space – FE). Testing the variational formulation with the rotational basis does* not *lead to the Newton-Euler equations of motion for the particle.*

Remark 7 *(Artificial saddle-point problem).* We want to mention that Glowinski et al. [14], Patankar et al. [28] apply a similar approach of extending the spaces. Due to the decoupling between the fluid and particle velocities in (30), (31) an explicit forcing strategy is commonly used by adding the Lagrange multiplier terms (28) and (29). The resulting system is often called *combined* momentum equations, cf. [45], [14]. The major drawback is the artificially created saddle-point structure by introduction of the LM which is typically solved by splitting the operators of the Navier-Stokes equation and the LM. A well defined fractional time stepping scheme needs to be defined in order to retain good approximation properties after the splitting.

2.5. Concluding remark

With regard to the Lemmata 1 and 2 we can conclude that the boundary integral formulation of the FVM preserves the coupling between fluid and particle degrees of freedom. In contrast, the volume integral formulation of the FEM leads to a decoupling. The crucial term causing the different outcome of the extension in (26), (27) compared to (30), (31) is the velocity-dependent part of the stress tensor, i.e. $\nabla \mathbf{u} + \nabla \mathbf{u}^T$. For the finite volume formulation it reads

$$a_{\mathrm{FV}}^{\mathrm{Cpl}}(\mathbf{u}, \mathbf{v}) := \int_{\partial P} \mu \left[\nabla \mathbf{u} + \nabla \mathbf{u}^T\right] \mathbf{n} \cdot \mathbf{v} \, ds. \tag{32}$$

The corresponding term of the finite element formulation reads

$$a_{\mathrm{FE}}^{\mathrm{Cpl}}(\mathbf{u}, \mathbf{v}) := \int_{P} \mu \left[\nabla \mathbf{u} + \nabla \mathbf{u}^T\right] : \nabla \mathbf{v} \, d\mathbf{x}. \tag{33}$$

It should be noted that the gradients $\left[\nabla \mathbf{u} + \nabla \mathbf{u}^T\right] \mathbf{n} \mid_{\partial P}$ in normal direction into the fluid depend on *both*, the velocity of the fluid *and* of the particle. Consequently the coupling between the degrees of freedom of the fluid and the particle is established in case of the boundary integral formulation of the FVM, but was canceled in case of the FEM:

$$(\nabla \mathbf{u} + \nabla \mathbf{u}^T) \, \mathbf{n} \mid_{\partial P} \neq \mathbf{0} \Longrightarrow a_{\mathrm{FV}}^{\mathrm{Cpl}}(\mathbf{u}, \mathbf{v}) \neq 0, \tag{34}$$

$$(\nabla \mathbf{u} + \nabla \mathbf{u}^T) \mid_{P} = \mathbf{0} \Longrightarrow a_{\mathrm{FE}}^{\mathrm{Cpl}}(\mathbf{u}, \mathbf{v}) = 0. \tag{35}$$

Remark 8. The expression (33) comprising $\nabla \mathbf{v}$ instead of $\mathbf{D}[\mathbf{v}]$ facilitates the comparison between $a_{\mathrm{FV}}^{\mathrm{Cpl}}(\mathbf{u}, \mathbf{v})$ and $a_{\mathrm{FE}}^{\mathrm{Cpl}}(\mathbf{u}, \mathbf{v})$. We will utilize it for all further considerations. It can be derived from the symmetry of $\mathbf{S} := \nabla \mathbf{u} + \nabla \mathbf{u}^T$ applying the following transformation for the tensor product:

$$\mathbf{S} : \nabla \mathbf{v} = \mathrm{tr}(\mathbf{S} \, \nabla \mathbf{v}^T) = \mathrm{tr}(\mathbf{S}^T \, \nabla \mathbf{v}) = \mathrm{tr}(\mathbf{S} \, \nabla \mathbf{v}) = \mathbf{S} : \nabla \mathbf{v}^T \implies \mathbf{S} : \mathbf{D}[\mathbf{v}] = \mathbf{S} : \nabla \mathbf{v}.$$

3. Numerical formulation

The aim of this section is to describe the general components for the discretization of problem (25) - (27) in time and space. This includes the definition of according discrete versions of the extended spaces introduced in Section 2.3. We want to emphasize that the described formulation is applicable to two- and three-dimensional space.

3.1. Discretization in time: updating the location of the particle

Most methods which treat the rigid body motion via Lagrange multiplier or other additional external force terms need to solve a saddle-point system. Typically an operator splitting approach is applied to solve bulk equations and particle equations separately, as in [33], [2], [42] or also [39], [38]. This yields a decoupling of the computation of the fluid solution and the solution for the particles. In order to guarantee a numerically stable solving procedure the splitting scheme needs to be defined carefully. Special time stepping schemes are applied to assure a good transfer of the interacting forces.

Since our fully-coupled approach implements the interaction forces between particles and the fluid in a strong and stable way, all variables of the fluid and the particles can be computed at once. For each time step the complete discrete non-linear system is solved applying a suitable Newton iteration scheme. In particular, no operator splitting is necessary.

For the discretization of the time derivative an implicit Euler scheme is applied. It possesses only first order accuracy, but can easily be replaced by an appropriate scheme of higher order. Since the particles are modeled in a Lagrangian frame,

the new location of the particles and the interface needs to be updated after each time step. A potential problem can arise if nodes within a particle will be part of the fluid grid in the next time step. Our scheme does not additionally account for that circumstance and simply utilizes the velocity of the rigid body at the according location. Our numerical results show that this implementation near the interface is sufficient and did not have negative impact to the global discretization error. For higher Reynolds numbers and deformable interfaces this strategy presumably needs to be adapted.

3.2. Discretization in space: discrete extended spaces

For the discretization in space we define suitable discrete function spaces $\mathcal{U}_h^{\text{RBM}} \subset \mathcal{U}^{\text{RBM}}$ and $\mathcal{V}_h^{\text{RBM}} \subset \mathcal{V}^{\text{RBM}}$. They will be based on the standard finite element and finite volume spaces defined on the background mesh of the domain Ω.

3.2.1. Unconstrained finite element and finite volume spaces

Let $\mathcal{T}_h$ be a triangulation of Ω with related grid points $\mathcal{X}_h := \{\vec{x}_i\}_{i=1}^N$ and $\mathcal{B}_h := \{B_i\}_{i=1}^N$ be a dual partition of Ω for which each control volume $B_i \subset \mathcal{B}_h$ is associated to exactly one grid point $\vec{x}_i \in B_i$, i.e. satisfying $\vec{x}_i \in B_i$. (A concrete definition of the B_i will be given in Section 4.) By means of some nodal functions φ_i, φ_i^*, both satisfying

$$\varphi_i(\vec{x}_j) = \varphi_i^*(\vec{x}_j) = \delta_{ij} \quad \forall \vec{x}_i \in \mathcal{X}_h$$

we define the basis $\Phi_h := \{\varphi_i \mid \vec{x}_i \in \mathcal{X}_h\}$ and $\Phi_h^* := \{\varphi_i^* \mid \vec{x}_i \in \mathcal{X}_h\}$. For the purpose of generality we keep the particular shape of the functions φ_i, φ_i^* unspecified. By means of the common characteristic functions

$$\chi_i(\vec{x})|_{B_i} = 1, \qquad \chi_i(\vec{x}) = 0, \quad \text{else,}$$

for all $B_i \in \mathcal{B}_h$, we can define a bijective mapping $\Pi : \Phi_h \to \Pi(\Phi_h)$, $\Pi(\varphi_i) := \chi_i$ of shape functions φ_i onto its related characteristic functions χ_i. We obtain $\mathcal{V}_h = \text{span}(\Pi(\Phi_h)^d)$ and define $\mathcal{U}_h := \text{span}(\Phi_h^d)$ and $N := \dim(\Phi_h) = \dim(\Pi(\Phi_h))$. Let further $\mathcal{P}_h = \text{span}(\Phi_h^*)$ be the unconstrained space for the pressure field. By means of the index set $\mathcal{I}_f \subset \{1, ..., N\}$ for all vertices belonging to Ω_f we define the discrete subspaces $\mathcal{U}_h^f := \text{span}\{\varphi_i \mathbf{e}_k\}_{k=1, i \in \mathcal{I}_f}^d$ of $\mathcal{U}^f$ and can rewrite $\mathcal{V}_h^f = \text{span}\{\chi_i \mathbf{e}_k\}_{k=1, i \in \mathcal{I}_f}^d$.

3.2.2. Extended finite element and finite volume spaces

For the discrete spaces $\mathcal{U}_h^{\text{lin}}$ and $\mathcal{V}_h^{\text{lin}}$ we define the two functions

$$\varphi_{P_h}(\vec{x}) := \sum_{\vec{x}_i \in P} \varphi_i(\vec{x}) \quad \text{and} \quad \chi_{P_h}(\vec{x}) := \sum_{\vec{x}_i \in P} \chi_{B_i}(\vec{x}) \tag{36}$$

which gives

$$\mathcal{U}_h^{\text{lin}} := \text{span}\{\varphi_{P_h} \mathbf{e}_k\}_{k=1}^d \quad \text{and} \quad \mathcal{V}_h^{\text{lin}} := \text{span}\{\chi_{P_h} \mathbf{e}_k\}_{k=1}^d. \tag{37}$$

Furthermore, we introduce a piecewise constant approximation for $\mathbf{r}(\vec{x})$ by

$$\bar{\mathbf{r}}(\vec{x}) := \mathbf{r}_i := \vec{x}_i - x_c, \quad \text{for } \vec{x} \in \text{supp}(\varphi_i). \tag{38}$$

Based on $\mathbf{r}_i$ and

$$\boldsymbol{\varphi}_{P_h}^{\mathbf{r}}(\vec{x}) := \sum_{\vec{x}_i \in P} \varphi_i(\vec{x}) \mathbf{r}_i \quad \text{and} \quad \boldsymbol{\chi}_{P_h}^{\mathbf{r}}(\vec{x}) := \sum_{\vec{x}_i \in P} \chi_{B_i}(\vec{x}) \mathbf{r}_i$$

the according discrete spaces $\mathcal{U}_h^{\text{rot}}$ and $\mathcal{V}_h^{\text{rot}}$ are defined by

$$\mathcal{U}_h^{\text{rot}} := \text{span}\{\mathbf{e}_k \times \boldsymbol{\varphi}_{P_h}^{\mathbf{r}}\}_{k=1}^d \quad \text{and} \quad \mathcal{V}_h^{\text{rot}} := \text{span}\{\mathbf{e}_k \times \boldsymbol{\chi}_{P_h}^{\mathbf{r}}\}_{k=1}^d. \tag{39}$$

Due to (16) we need degrees of freedom on the boundary of the interface. Therefore, we first define the slightly enlarged domain

$$\Omega_{f,p} := \Omega_f \cup T_{\text{Cut}} \qquad \text{with} \quad T_{\text{Cut}} := \bigcup_{T \cap \partial P \neq \emptyset} T,$$

which contains in addition to the vertices in Ω_f all vertices lying on cut elements, i.e. also those lying inside P and close to the interface. The discrete spaces for the pressure are finally defined based on $\chi_{i,p}(\vec{x}) := \chi_i(\vec{x})$ and $\chi_{i,p}(\vec{x}) = 0$ for $\vec{x} \notin \Omega_{f,p}$ by

$$\mathcal{P}_h^{\text{RBM}} := \text{span}\{\varphi_i^* \mid \vec{x}_i \in \Omega_{f,p}\} \quad \text{and} \quad \mathcal{Q}_h^{\text{RBM}} := \text{span}\{\chi_{i,p} \mid \vec{x}_i \in \Omega_{f,p}\}.$$
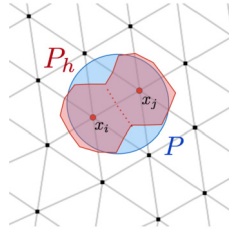
Fig. 2. Minimal discrete representation P_h of a particle $P \subset \Omega$ for the barycenter FVM.

Recall that according to (36) the discrete representation P_h of P with respect to $\mathcal{B}_h$ reads

$$P_h = \bigcup_{\vec{x}_i \in P} B_i. \tag{40}$$

Examples for the discrete particle are depicted in Figs. 2 and 4(a) for the *barycenter* FVM.

3.3. Transformation of the discrete system

We will only derive the transformations for the operator $a_{\mathrm{FV}}(\cdot, \cdot)$, because the same operations can be applied for the adaption of the mass balance and pressure term, respectively. We start with the discrete velocity field $\mathbf{u}(\vec{x}) = \sum_{i=1}^{N} \mathbf{u}_i \varphi_i(\vec{x})$, $\varphi_i(\vec{x}) \in \Phi_h$, $\mathbf{u}_i \in \mathbb{R}^d$. Let

$$\mathbf{A}\mathbf{u} = \mathbf{f} \tag{41}$$

be the linear system of the unconstrained finite volume method on Ω without particles. It is $\mathbf{A} \in \mathbb{R}^{M \times M}$, with $M = dN$. We will use the sub-matrices

$$\mathbf{A}_{i,j} := a_{\mathrm{FV}}(\varphi_j(\vec{x})\,\mathsf{Id},\, \chi_i(\vec{x})\,\mathsf{Id}) \in \mathbb{R}^{d \times d},$$

which contain the coupling entries between the vertices $\vec{x}_i, \vec{x}_j \in \mathcal{X}_h$ for all velocity components, with identity matrix $\mathsf{Id} \in \mathbb{R}^{d \times d}$. Since $\mathcal{U}_h^{\mathrm{RBM}}$ and $\mathcal{V}_h^{\mathrm{RBM}}$ are derived from the basis Φ_h and $\Pi(\Phi_h)$, it is evident that the related discrete linear system

$$\mathbf{A}^* \mathbf{u} = \mathbf{f}^*$$

can be formulated as some transformation of (41): With regard to (37) the matrix $\mathbf{A}^*$ is generated by summing up rows and columns of $\mathbf{A}$. For the sub-matrices containing couplings to the translational component $\mathbf{U}$ it follows from (37) that

$$\mathbf{A}_{\mathbf{U},j} = a_{\mathrm{FV}}(\varphi_j(\vec{x})\,\mathsf{Id},\, \chi_{P_h}\,\mathsf{Id}) = \sum_{x_i \in P \cap T_{\mathrm{Cut}}} \mathbf{A}_{i,j}, \quad \vec{x}_j \in \Omega_f, \tag{42}$$

$$\mathbf{A}_{i,\mathbf{U}} = a_{\mathrm{FV}}(\varphi_{P_h}\,\mathsf{Id},\, \chi_i(\vec{x})\,\mathsf{Id}) = \sum_{x_j \in P \cap T_{\mathrm{Cut}}} \mathbf{A}_{i,j}, \quad \vec{x}_i \in \Omega_f. \tag{43}$$

Remark that only vertices $\vec{x}_i \in P \cap T_{\mathrm{Cut}}$ are taken into account for the summation in (42) and (43), because the coupling entries with respect to inner nodes cancel out. Therefore, the discrete scheme is consistent with Remark 5 and the property (35).

With regard to (39) the transformation relies on the local radial directions $\mathbf{r}_i$. We introduce the *local rotation matrix* associated to a vector $\mathbf{r}_i$ as

$$\mathsf{R}_i := \begin{pmatrix} -\mathbf{r}_i[2] & 0 \\ \mathbf{r}_i[1] & 0 \end{pmatrix}, \quad \mathbf{r}_i \in \mathbb{R}^2 \quad \text{and} \quad \mathsf{R}_i := \begin{pmatrix} 0 & -\mathbf{r}_i[3] & \mathbf{r}_i[2] \\ \mathbf{r}_i[3] & 0 & -\mathbf{r}_i[1] \\ -\mathbf{r}_i[2] & \mathbf{r}_i[1] & 0 \end{pmatrix}, \quad \mathbf{r}_i \in \mathbb{R}^3. \tag{44}$$

Considering Remark 5 and (35) the summation over all inner control volumes with $B_i \cap \partial P = \emptyset$ needs to cancel for the rotational component as well. An appropriate approximation of the discrete integrals yields the desired consistency. For the sub-matrices related to the rotational component $\boldsymbol{\omega}$ we get

$$\mathbf{A}_{\boldsymbol{\omega},j} = a_{\mathrm{FV}}(\varphi_j(\vec{x})\,\mathsf{Id},\, \sum_{x_i \in P} \chi_i\,\mathsf{R}_i) = \sum_{x_i \in P \cap T_{\mathrm{Cut}}} \mathsf{R}_i^T \mathbf{A}_{i,j}, \quad \vec{x}_j \in \Omega_f, \tag{45}$$

$$\mathbf{A}_{i,\boldsymbol{\omega}} = a_{\mathrm{FV}}(\sum_{x_j \in P} \varphi_j\,\mathsf{R}_j,\, \chi_i(\vec{x})\,\mathsf{Id}) = \sum_{x_j \in P \cap T_{\mathrm{Cut}}} \mathbf{A}_{i,j}\,\mathsf{R}_j, \quad \vec{x}_i \in \Omega_f. \tag{46}$$

The diagonal entries finally read

$$\mathbf{A}_{\mathbf{U},\mathbf{U}} = \sum_{i,j} \mathbf{A}_{i,j}, \quad \text{and} \quad \mathbf{A}_{\boldsymbol{\omega},\boldsymbol{\omega}} = \sum_{i,j} \mathsf{R}_i^T \mathbf{A}_{i,j} \mathsf{R}_j, \quad \vec{x}_i, \vec{x}_j \in P \cap T_{\text{Cut}}.$$

3.4. Concluding remarks

In analogy to the definition of the continuous spaces the discrete spaces inherit a projection onto the corresponding spaces. This has some preferable consequences for the algorithmic implementation and the numerical properties. We shall summarize them by means of the following remarks.

Remark 9 (*Compability*). The projection onto rigid body motion yields a reduced discrete system, i.e.

$$\dim(\mathcal{U}_h^{\text{RBM}}) \le \dim(\mathcal{U}_h) \quad \text{and} \quad \dim(\mathcal{V}_h^{\text{RBM}}) \le \dim(\mathcal{V}_h).$$

Therefore, no additional degrees of freedom need to be introduced during the assembling process.

Remark 10 (*Conformity*). Due to (38) the shape functions for the rotational spaces are defined as piecewise constant rotation on its support. The resulting shape functions are simply re-weighted shape functions of the original space with special, rotational weighting for each coordinate direction. Therefore, $\mathcal{U}_h^{\text{rot}}$ and $\mathcal{V}_h^{\text{rot}}$ consist of distinguished linear combinations of the Euclidean basis. We can conclude that $\mathcal{U}_h^{\text{lin}}$, $\mathcal{U}_h^{\text{rot}} \subset \mathcal{U}_h$ and $\mathcal{V}_h^{\text{lin}}$, $\mathcal{V}_h^{\text{rot}} \subset \mathcal{V}_h$ which finally yields

$$\mathcal{U}_h^{\text{RBM}} \subset \mathcal{U}_h \quad \text{and} \quad \mathcal{V}_h^{\text{RBM}} \subset \mathcal{V}_h. \tag{47}$$

In particular, the same assembling and solving algorithms can be applied as for the unconstrained problem on the Eulerian mesh for the whole domain Ω. The assembling for the rotational weights can be treated as a post processing, as derived in (45), (46).

In Section 5 we will discuss the benefits of the relation (47) for the numerical analysis of the developed scheme.

Remark 11 (*Conservativity*). The conservation of momentum and mass are locally and globally satisfied as far as they are satisfied by the original discrete scheme. It should be emphasized that the discrete velocity field exerts a rigid body motion only on the reduced domain $T_{\text{Inner}} := P_h \setminus T_{\text{Cut}}$, i.e. $\mathbf{u}(\vec{x})|_{T_{\text{Inner}}} = \mathbf{U} + \boldsymbol{\omega} \times \bar{\mathbf{r}}(\vec{x})$, but not on P_h.

Remark 12 (*Rigid particle as rotating finite volumes*). Neglecting the rotational component and choosing $\mathcal{U}^{\text{RBM}} = \mathcal{U}^f \oplus \mathcal{U}^{\text{lin}}$ as ansatz space and $\mathcal{V}^{\text{RBM}} = \mathcal{V}_h^f \oplus \mathcal{V}^{\text{lin}}$ as test space the equations (25), (26) correspond to the usual finite volume scheme applied to the special partition containing the control volume P_h.

Remark 13 (*Discrete regularity*). For the discrete spaces (37) and (39) we have to reconsider Remark 3: For a given triangulation $\mathcal{T}_h$ of Ω at least two vertices $\vec{x}_i, \vec{x}_j \in P$, $\vec{x}_i \ne \vec{x}_j$, are necessary for the local independence of the related shape functions. If only one vertex $\vec{x}_i$ is contained in P we get $\mathsf{R}_{\vec{x}} \equiv \mathsf{R}_i$ for all $\vec{x} \in P_h$.

With regard to the definition in (40) the minimal size of the discrete particle P_h with respect to a triangulation $\mathcal{T}_h$ will be the union of the two control volumes related to the inner vertices of the particle P, as depicted in Fig. 2 for the *barycenter* FVM (see Section 4).

We shall summarize the consideration of the last remark in the following corollary:

Corollary 3. *A necessary condition for the regularity of the discrete scheme on $\mathcal{U}_h^{RBM}$ and $\mathcal{V}_h^{RBM}$ is the existence of at least two vertices $\vec{x}_i, \vec{x}_j \in P$, $\vec{x}_i \ne \vec{x}_j$.*

We will show in Section 5 that the condition formulated in Corollary 3 is even sufficient for the regularity and stability of the operator $a_{\text{FV}}(\cdot, \cdot)$ on $\mathcal{U}_h^{\text{RBM}} \times \mathcal{V}_h^{\text{RBM}}$.

4. FVM and FEM for particulate flow

So far, we introduced the general extended discrete spaces $\mathcal{U}_h^{\text{RBM}}$ and $\mathcal{V}_h^{\text{RBM}}$ with respect to an arbitrary triangulation $\mathcal{T}_h$ and any dual mesh $\mathcal{B}_h$ of Ω. In Section 4.1 we will apply that general scheme to the so called *barycenter* FVM. The implementation was done within the software framework *UG4* [43]. Herein the finite volume discretization for the Navier-Stokes equations is based on the stabilized scheme of Reichert and Wittum [32] and Nägele and Wittum [25]. Collocated and equal first order spaces for the velocity and pressure are employed and additional stabilization terms are introduced in the mass balance equation. For details concerning the implementation within *UG4* we shall refer to [24], [25].
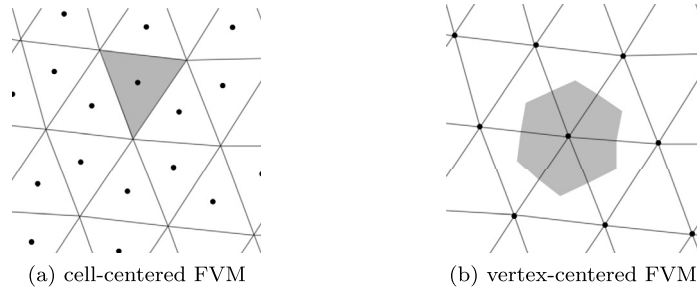
(a) cell-centered FVM	(b) vertex-centered FVM

Fig. 3. Mesh and dual mesh of the (a) cell-centered and (b) vertex-centered FVM.

4.1. A stable FVM for particulate flow

We will apply the general approach described in Section 3 to a so called *vertex-centered* finite volume method using *barycenter* finite volumes. The definition of the dual mesh of Ω on which the balance laws are stated is a crucial step when constructing the FVM. Based on that a FVM can generally be divided into two different categories: Choosing $\mathcal{B}_h \equiv \mathcal{T}_h$ corresponds to a FVM with unknowns associated to each *cell* (= control volume) $T \in \mathcal{T}_h$ and is accordingly denoted by *cell-centered* FVM, see Fig. 3(a).

The second category of FVM are so called *vertex-centered* FVM. The control volumes are constructed around each vertex of the given triangulation $\mathcal{T}_h$. The most famous dual mesh is the *Voronoi diagram* based on the special case of a Delaunay triangulation $\mathcal{T}_h$. The edges of the control volumes intersect the edges of the elements in its midpoint and in orthogonal direction. A further example for a dual mesh are the *barycenter* control volumes. The discrete scheme was first introduced by Bank and Rose [3] and Chen [8] as so called *box method*. For the construction of the dual mesh in two dimensions the midpoints of all edges of triangles which share the same vertex are connected with the barycenter of all associated triangles, as depicted in Fig. 3(b). All numerical simulations showed in Section 6 were conducted using the *barycenter* FVM.

With P_h as defined in (40) and the corresponding barycenter control volumes B_i the FV discretization of (21) and (22) reads

$$M_{P_h} \frac{d}{dt} \mathbf{U} - \int_{\partial P_h} \boldsymbol{\sigma}(\vec{x}) \, \mathbf{n} \, d\mathbf{s} = M_{P_h} \mathbf{g},$$

(48)

$$I_{P_h} \frac{d}{dt} \boldsymbol{\omega} - \int_{\partial P_h} \bar{\mathbf{r}}(\vec{x}) \times \boldsymbol{\sigma}(\vec{x}) \, \mathbf{n} \, d\mathbf{s} = \mathbf{0}.$$

(49)

Equations (48), (49) are nothing else but the discretized version of the Newton-Euler equations (4) of a particle. The shape of ∂P_h for the barycenter FVM is depicted in Fig. 4(a).

4.2. Relating FVM and FEM

In Section 2 the FVM was described as a bilinear form by introducing a *virtual* second argument into the balance equations. Applying mathematically rigorous arguments a FVM can be derived from a so called *generalized variational formulation* of the PDEs (1)–(2). In [4] that was done for the convection-diffusion equation. That close relation between FEM and FVM is well known and commonly used to derive theoretical statements for a FVM. For the special choice of a barycenter dual mesh and piecewise linear spaces $\mathcal{P}^1(\mathcal{T}_h)$ the stiffness matrix of the Laplacian (presuming piecewise constant coefficient on each element) is even identical to the corresponding finite element matrix. That was first proven by Bank and Rose [3] for the two-dimensional case and later also for arbitrary dimension by Chen [8], Xu and Zou [49] and Hackbusch [17]. Similar arguments were applied in [51] for the proof of identical schemes for the linear Stokes equations in order to derive corresponding stability and convergence results. We will follow similar arguments in Section 5 to prove the stability of the scheme derived in Section 3.

The essential component for the barycenter FVM to be identical to a FEM is the choice of the midpoints of the edges for the construction of the barycenter control volumes. We want to formulate that important finding here again for two reasons: first, the identification will directly lead to a FEM for particulate flow, see Section 4.3. In particular, the coupling forces in (33) will not cancel. And second, the identification will serve us for the theoretical analysis of the described FVM for particulate flow in Section 5.

Lemma 3 ($\mathcal{P}^1(\mathcal{T}_h)$-*identity of the Laplace operator*). *Let $\mathcal{T}_h$ be a triangulation of a polyhedral domain $\Omega \subset \mathbb{R}^d$ and $\mathcal{B}_h$ the* barycenter *dual mesh. For $u \in \mathcal{P}^1(\mathcal{T}_h)$, nodal basis functions $\varphi_i \in \mathcal{P}^1(\mathcal{T}_h)$ and associated $B_i \in \mathcal{B}_h$ the following* local *identity is satisfied:*

$$- \int\limits_{\partial B_i \cap T} \nabla u \cdot \boldsymbol{n} \, d\boldsymbol{s} = \int\limits_{T} \nabla u \cdot \nabla \varphi_i \, d\boldsymbol{x},$$

for all $T \in \mathcal{T}_h$. This gives the global identity

$$- \sum_i \int\limits_{\partial B_i} \nabla u \cdot \boldsymbol{n} \, v_i \, d\boldsymbol{s} = \int\limits_{\Omega} \nabla u \cdot \nabla v \, d\boldsymbol{x}.$$

for each $v = \sum_i v_i \varphi_i \in \mathcal{P}^1(\mathcal{T}_h)$.

By means of Lemma 3 the identity of the coupling terms (32) and (33) of a FVM and FEM, respectively, can directly be derived:

Corollary 4. *With the assumptions of Lemma 3, $\boldsymbol{u}, \boldsymbol{v} \in [\mathcal{P}^1(\mathcal{T}_h)]^d$ and the bijective mapping Π as defined in Section 3.2.1 it is*

$$a_{FV}^{Cpl}(\boldsymbol{u}, \Pi(\boldsymbol{v})) = a_{FE}^{Cpl}(\boldsymbol{u}, \boldsymbol{v}). \tag{50}$$

Due to (50) the coupling term of the finite element scheme does not cancel in the discrete case. This enables us to formulate a FEM based on the described extension of the test space, which is fully-coupled and stable without additional Lagrange multiplier.

4.3. A non-Lagrange multiplier FEM for particulate flow

By means of Corollary 4 the FE scheme for particulate flow can be derived easily for the symmetrically defined discrete spaces $\mathcal{U}_h^{\text{RBM}} \times \mathcal{P}_h^{\text{RBM}}$. The missing component is an analogue result of Corollary 4 for the pressure term. Application of Lemma 3 directly gives

$$\sum_i \int\limits_{\partial B_i \cap T} p \, \mathbf{n} \cdot \Pi(\mathbf{v}) \, d\mathbf{s} = - \sum_i \int\limits_{\Omega} p \, \nabla \varphi_i \cdot \Pi(\mathbf{v}) \, d\mathbf{x} = - \int\limits_{\Omega} p \, \nabla \cdot \mathbf{v} \, d\mathbf{x}. \tag{51}$$

We can formulate the following FE discretization of (21) and (22):

$$M_{P_h} \frac{d}{dt} \mathbf{U} \cdot \mathbf{V} + \int\limits_{\hat{P}_h} \boldsymbol{\sigma}(\vec{x}) : \nabla(\varphi_{P_h} \mathbf{V}) \, d\mathbf{x} = M_{P_h} \, \mathbf{g} \cdot \mathbf{V}, \tag{52}$$

$$I_{P_h} \frac{d}{dt} \boldsymbol{\omega} \cdot \boldsymbol{\zeta} + \int\limits_{\hat{P}_h} \bar{\mathbf{r}}(\vec{x}) \times \boldsymbol{\sigma}(\vec{x}) : \nabla(\varphi_{P_h} \boldsymbol{\zeta}) \, d\mathbf{x} = 0. \tag{53}$$

Depending on the evaluation of the discrete integral over $\hat{P}_h$ the integral in (53) will generally differ from the one in (49). Furthermore, due to the definition of $\varphi_{P_h}(\vec{x})$ in (36) it is

$$\hat{P}_h = \text{supp}(\varphi_{P_h}) \neq P_h \, (\overset{(40)}{=} \bigcup_{\vec{x}_i \in P} B_i).$$

But by means of well known identities for the barycenter FVM, cf. [4], we get

$$\int\limits_{\hat{P}_h} \varphi_{P_h} \, d\mathbf{x} = \int\limits_{P_h} \chi_{P_h} \, d\mathbf{x} = M_{P_h}.$$

Therefore, the FEM solves for the unknowns $\mathbf{U}$ and $\boldsymbol{\omega}$ with respect to the same discrete masses.

4.4. FEM for particulate flow: interface with finite thickness

We recall that in the continuous case the coupling term (33) cancels due to the rigidity constraint. The situation essentially changes when solving the variational problem (12)–(13) for discrete spaces, see (52), (53). In order to investigate that observation in more detail we define the relevant subdomains T_{Inner} and T_{Cut}, cf. Fig. 4(b). For the discrete space it is

$$\nabla \mathbf{u} + \nabla \mathbf{u}^T \, |_{T_{\text{Inner}}} = \mathbf{0}, \quad \text{but} \quad \nabla \mathbf{u} + \nabla \mathbf{u}^T \, |_{T_{\text{Cut}}} \neq \mathbf{0}, \tag{54}$$
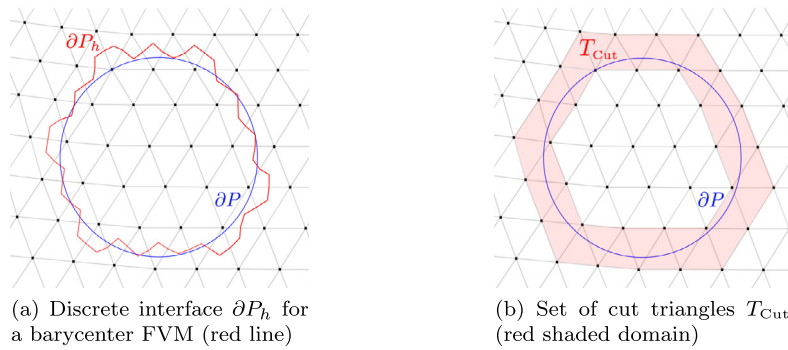
(a) Discrete interface ∂P_h for
a barycenter FVM (red line)

(b) Set of cut triangles T_{Cut}
(red shaded domain)

Fig. 4. Discrete representations of ∂P (blue line): (a) as interface ∂P_h (FVM) and (b) as boundary with finite thickness T_{Cut} (FEM).

which finally gives $a_{\mathrm{FE}}^{\mathsf{Cpl}}(\mathbf{u}, \varphi_{P_h}\mathbf{V}) \neq 0$. It can be stated more generally, that $\nabla\varphi_{P_h}|_{T_{\mathrm{Inner}}} = \mathbf{0}$ is a sufficient condition for the first equality in (54). This is always satisfied, if the finite element space $\{\varphi_i\}_{i=1}^N$ forms a *partition of unity*, i.e.

$$\sum_i \varphi_i(\vec{x}) \equiv 1 \qquad \forall\, \vec{x} \in \Omega. \tag{55}$$

The resulting finite element scheme can be interpreted as a discretization of a boundary with *finite thickness*: Let $\Gamma_\delta := T_{\mathrm{Cut}}$ be the boundary of finite thickness containing ∂P_h. We can rewrite the coupling term $a_{\mathrm{FE}}^{\mathsf{Cpl}}(\cdot, \cdot)$ as follows:

$$a_{\mathrm{FE}}^{\mathsf{Cpl}}(\mathbf{u}, \varphi_{P_h}\mathbf{V}) = \int_{\Gamma_\delta} \mu\,[\,\nabla\mathbf{u} + \nabla\mathbf{u}^T\,] : \nabla(\varphi_{P_h}\mathbf{V})\,d\mathbf{x} =: a_{\Gamma_\delta}(\mathbf{u}, \varphi_{P_h}\mathbf{V}). \tag{56}$$

Remark 5 directly yields the relation

$$\int_{\Gamma_\delta} \mu\,[\,\nabla\mathbf{u} + \nabla\mathbf{u}^T\,] : \nabla(\varphi_{P_h}\mathbf{V})\,d\mathbf{x} = \int_{\partial P_h} \mu\,[\,\nabla\mathbf{u} + \nabla\mathbf{u}^T\,]\,\mathbf{n}\cdot\mathbf{V}\,ds. \tag{57}$$

With interface force $\mathbf{f}$ defined as the stresses on the boundary, i.e. $\mathbf{f} = \mu\,[\,\nabla\mathbf{u} + \nabla\mathbf{u}^T\,]\,\mathbf{n}$, the FEM can be interpreted as a certain *diffusive-interface* method in the following sense:

Remark 14 (*Direct forcing using surface delta functions*). The set of cut triangles T_{Cut} resembles a layer of mean thickness h, which acts as a boundary of finite thickness as depicted in Fig. 4(b). The class of *diffusive-interface methods* [33], [9], [36], [37] similarly treats the interface as domain of finite thickness: so called *surface delta functions* are introduced in order to solve the bulk equation on a layer of thickness $\epsilon > 0$ containing the interface. That approach simplifies the implementation of the boundary forces on a moving interface. In the context of diffusive-interface methods the following requirement for a discrete surface delta function δ_Γ is commonly stated:

$$\int_\Omega \mathbf{f}\,\delta_\Gamma\,d\mathbf{x} = \int_\Gamma \mathbf{f}\,ds,$$

with a prescribed force $\mathbf{f}$ on the interface. There are further methods like IBM or *direct forcing* methods [39], [38] which introduce so called *discrete delta functions* in order to transform the interface integral for the immersed boundary into a volume integral.

Regarding (57) an extension by arbitrary basis functions satisfying (55) naturally inherits a diffusive-interface method on the according layer T_{Cut}. Therefore, the extended spaces can be interpreted as suitably chosen surface delta functions.

With regard to Remark 14 the crucial question will be, how to choose φ_{P_h} appropriately, i.e. such that the boundary integral of the related FVM is a good approximation to Γ. As we will see in the next section (recall also Fig. 4(a)) the extension by φ_{P_h} possesses only minor approximation properties and needs to be adapted. The identity to FVM gives a good guideline to define the optimal surface delta function. A suitable adaption for the common linear finite element space $\mathcal{P}^1(\mathcal{T}_h)$ will be derived in a separate work forthcoming paper.

5. Numerical analysis

For the numerical analysis of the derived schemes (FVM derived in Section 4.1 and FEM derived in Section 4.3) we will investigate the stationary linear Stokes equations being a simplified form of the general Navier-Stokes equations which describe the flow of a highly viscous fluid. We define the common bilinear forms

$$a(\mathbf{u}, \mathbf{v}) := \int_{\Omega} 2\,\mu\,\mathbf{D}[\mathbf{u}] : \mathbf{D}[\mathbf{v}]\,d\mathbf{x}, \qquad b(p, \mathbf{v}) := -\int_{\Omega} p\,\nabla \cdot \mathbf{v}\,d\mathbf{x}$$

and get the following discrete saddle-point problem: Find $\mathbf{u} \in \mathcal{U}_h^{\text{RBM}}$, $p \in \mathcal{P}_h^{\text{RBM}}$ s.t.

$$a(\mathbf{u}, \mathbf{v}) + b(p, \mathbf{v}) = (\mathbf{g}, \mathbf{v}) \qquad \forall\,\mathbf{v} \in \mathcal{U}_h^{\text{RBM}}, \tag{58}$$

$$b(q, \mathbf{u}) = 0 \qquad \forall\,q \in \mathcal{Q}_h^{\text{RBM}}. \tag{59}$$

Due to Corollary 4 and (51) the bilinear forms for the corresponding finite volume scheme are identical on the respective spaces. Therefore we chose the unified notation $a(\cdot, \cdot)$ and $b(\cdot, \cdot)$.

5.1. Stability

For the stability of (58), (59) we need to show coercivity of the operator $a(\cdot, \cdot)$ and the inf-sup condition for $b(\cdot, \cdot)$. Our approach of modeling via test spaces yields a scheme for particulate flow that comprises solely the original bilinear form. Therefore, we need to show its coercivity with respect to the extended spaces $\mathcal{U}_h^{\text{RBM}} \times \mathcal{P}_h^{\text{RBM}}$. Because of the coercivity of the finite element operator $a(\mathbf{u}, \mathbf{v})$ on the according continuous spaces, we can immediately state the sought result.

Lemma 4 *(Coercivity). For $a(\cdot, \cdot)$ there holds*

$$a(\boldsymbol{u}, \boldsymbol{u}) \geq c\,\|\boldsymbol{u}\|_1^2 \qquad \text{for all } \boldsymbol{u} \in \mathcal{U}_h^{\text{RBM}},$$

with suitable constant $c > 0$ independent of $\boldsymbol{u}$ and norm $\|\cdot\|_1$ on $\boldsymbol{H}_0^1(\Omega)$.

Proof. Application of *Korn's First Inequality*, [22], yields

$$\int_{\Omega} 2\,\mu\,\mathbf{D}[\mathbf{u}] : \mathbf{D}[\mathbf{u}]\,d\mathbf{x} \geq c\,\|\mathbf{u}\|_1^2$$

for $\mathbf{u} \in \mathbf{H}_0^1(\Omega)$ satisfying homogeneous boundary conditions on $\partial\Omega$. Because of $\mathcal{U}_h^{\text{RBM}} \subset \mathcal{U}_h$, see (47), coercivity is satisfied on the closed subspace $\mathcal{U}_h^{\text{RBM}}$ of $\mathbf{H}_0^1(\Omega)$. □

For the derivation of the inf-sup condition for the particulate Stokes problem (58), (59) we assume that the bilinear form $b(\cdot, \cdot)$ satisfies the inf-sup condition on the unconstrained spaces $\mathcal{U}_h \times P_h$. This assumption is reasonable for the following reason: Finite element schemes often choose lower order spaces for the pressure in order to satisfy the inf-sup condition. With regard to the finite volume scheme applied in this paper additional stabilization terms are introduced. Even though an inf-sup condition was not derived theoretically so far we can assume stability for this scheme. Therefore, both approaches provide a stable discretization scheme on the unconstrained spaces.

We will pursue the following general reasoning: As first consequence, the inf-sup condition is equally satisfied on the domain $\Omega \setminus T_{\text{Inner}}$. We introduce the notations $\mathcal{U}_h^*$ and $\mathcal{P}_h^*$ for the related unconstrained spaces on $\Omega \setminus T_{\text{Inner}}$ and want to mention the following two statements for our conclusion:

(i) The *outer* boundary of $\Omega \setminus T_{\text{Inner}}$ is composed by $\partial\Omega_f = \partial\Omega \cup \partial T_{\text{Inner}}$ and the particulate Stokes problem with respect to the extended spaces corresponds to an unconstrained Stokes problem on $\Omega \setminus T_{\text{Inner}}$ but *without* homogeneous boundary conditions on $\partial T_{\text{Inner}}$.

(ii) The following relations hold: $\mathcal{U}_h^{\text{RBM}} \supset \mathcal{U}_h^*$ and $\mathcal{P}_h^{\text{RBM}} = \mathcal{P}_h^*$.

By means of (i) and (ii) the inf-sup condition for the extended spaces now immediately follows:

Lemma 5 *(Inf-sup condition). For $b(\cdot, \cdot)$ there holds*

$$\inf_{p \in \mathcal{P}_h^{\text{RBM}} \setminus \{0\}} \sup_{\boldsymbol{u} \in \mathcal{U}_h^{\text{RBM}} \setminus \{0\}} \frac{b(p, \boldsymbol{u})}{\|\boldsymbol{u}\|_{\mathcal{U}_h^{\text{RBM}}} \|p\|_{\mathcal{P}_h^{\text{RBM}}}} \geq \inf_{p \in P_h^* \setminus \{0\}} \sup_{\boldsymbol{u} \in \boldsymbol{U}_h^* \setminus \{0\}} \frac{b(p, \boldsymbol{u})}{\|\boldsymbol{u}\|_{\mathcal{U}_h^*} \|p\|_{\mathcal{P}_h^*}} \geq \gamma > 0,$$

with suitable constant $\gamma > 0$ independent of $\boldsymbol{u}$ and p.

Fig. 5. Angles β_i, β_j of the zig-zag shape of ∂P_h (red line); interface ∂P (blue line). (For interpretation of the colors in the figure(s), the reader is referred to the web version of this article.)

The Lemmata 4 and 5 imply that the particulate Stokes problem (58), (59) derived from a stable discretization scheme has a unique solution.

Remark 15. With regard to Remark 14 we can argue that the straightforward proofs for coercivity and inf-sup stability are due to a *suitable choice* of an according surface delta function. In particular, it satisfies $\varphi_{P_h} \mathbf{e}_i \subset \mathcal{U}_h$. It should be emphasized that most methods introduce *artificial* forcing terms to the discretized momentum equation. In case of common diffusive-interface methods or direct forcing strategies [39] the introduced delta functions in general do *not* satisfy $\delta_\Gamma \mathbf{e}_i \subset \mathcal{U}_h$. The fictitious domain method of [14] introduces new variables as Lagrange multiplier. In that case, the crucial condition for a stable system is an additional inf-sup condition for the system including the LM equations. Constructing a suitable LM space is not easy. Therefore, proving the stability of the system is not straightforward and has not been done so far.

5.2. Error analysis

The discretization employs the standard shape functions in space on the Eulerian grid $\mathcal{T}_h$. Therefore, the degrees of freedom are located in the original vertices and the derived scheme does not sharply account for the interface. This is equivalent to a certain *smearing* of the forces being exerted by the real interface which leads to a lack of consistency: Due to the definition of the discrete spaces on the extended domain the interface forces are computed on the discrete boundary $\partial P_h \neq \partial P$, see Fig. 4(a). We state the following properties of the relevant quantities:

Lemma 6. *For the discrete representation P_h in (40) and suitable parametric mappings $\gamma : [0, 2\pi] \to \partial P$ and $\gamma_h : [0, 2\pi] \to \partial P_h$ we obtain:*

$$\mathrm{vol}(P_h) \to \mathrm{vol}(P) \qquad \text{for } h \to 0, \tag{60}$$

$$\gamma_h(\theta) \to \gamma(\theta) \qquad \text{uniformly for } h \to 0, \ \theta \in [0, 2\pi], \tag{61}$$

but for all $\theta \in [0, 2\pi]$ lying inside the piecewise linear parts of ∂P_h it is

$$\gamma_h'(\theta) \nrightarrow \gamma'(\theta) \qquad \text{pointwise for } h \to 0. \tag{62}$$

Proof. The properties (60) and (61) can be derived easily. For the proof of (62) we want to refer to Fig. 5: By construction of the control volumes of the barycenter FV scheme the shape depicted by the red line is a *zig-zag* line, independent of the mean mesh size h. The jump in normal direction on the discrete boundary ∂P_h will not fall below an angle β. E.g. on two cut elements T_i and T_j it is β_i, $\beta_j \geq \beta$, as depicted in Fig. 5. That zig-zag line therefore produces a consistency error with respect to the interface condition. We obtain (62). □

A rigorous error analysis will be conducted in a forthcoming paper. With regard to Lemma 6 we simply want to mention the following: From the properties (60) and (61) we can at least state a certain *global consistency* with respect to the velocity of the particles: Since for the computation of the particle velocities the forces acting on a particle are integrated over the whole boundary ∂P_h, the local errors in the computation of the normal forces due to (62) are expected to smooth out. The numerical results for the velocity field presented in Section 6 support this reasoning. Due to (62), however, the approximation of the local forces will not converge to the real forces. In particular, the direction of the discrete forces deviate by a mean angle of $\beta/2$. Therefore, the discrete problem is not consistent with the continuous one and the overall approximation is diminished. This could be observed in the numerical tests, see Section 6. In particular, contrary to the velocity the computation of the local pressure near the interface depends on local gradients. Therefore, the *local inconsistency* in normal direction becomes relevant. As a consequence, oscillations in the solution of the pressure along the interface were observed, see Fig. 9.

The observed oscillations of the pressure were the main driving force for the enhancement of the described scheme and the development of an immersed boundary approach which represents the interface sharply. The adapted method together with a more detailed error analysis will be described in a forthcoming paper.

6. Numerical simulations

In this section we present the numerical results. We derived a fully-coupled method for the simulation of particulate flow for which the interaction between fluid and particles is fully inherited into the discrete system. Even though the scheme is formulated for two and three dimensions, we will show only two-dimensional computations. Results for the three-dimensional case will be presented in a forthcoming paper including a better approximation of the interface. For the solution of the non-linear Navier-Stokes equations a fix-point iteration is used. For more details we refer to [24]. The arising linear systems have been solved with a geometric multigrid solver as provided in the software framework *UG4*, cf.[43], using ILU as smoother and a BiCGSTAB solver for the solution on the coarsest grid.

6.1. Convergence study – flow around a fixed cylinder

We evaluated the performance of the derived scheme by studying its convergence properties. For that purpose we consider the well known benchmark of flow in a channel around a fixed cylinder as extensively studied e.g. by Schäfer and Turek [34]. For the two dimensional case a circle with radius $r = 0.05m$ and center $(0.2m, 0.2m)$ is placed in a channel with dimensions $H \times L = 0.41m \times 2.2m$. Dirichlet boundary conditions are given on the left and right parts of the outer boundary with a parabolic profile given by

$$u(0, y) = \frac{4y(H - y)}{H^2} U_m, \quad U_m = 0.3 \frac{m}{s}, \quad v(0, y) \equiv 0.$$

On the upper and lower parts of the outer boundary usual no-slip conditions are applied. The prescribed velocity profile yields the mean velocity $\overline{U} = \frac{2}{3} u(0, \frac{H}{2}) = 0.2 \frac{m}{s}$. For viscosity $\mu = 0.001 \frac{m^2}{s}$ the Reynolds number for the fluid is $Re = \frac{2r\overline{U}}{\mu} = 20$.

The computations were conducted on the mesh as depicted in Fig. 6(b). The red line indicates the immersed interface which provides the information for the discrete scheme. Due to the setting of the benchmark the motion of the particle is prescribed to zero, i.e. $\mathbf{U} = \boldsymbol{\omega} = \mathbf{0}$. Furthermore, we used the boundary fitted mesh of Fig. 6(a) for comparison of our results with reference computations of an exact interface representation. Plots of the computed velocity and pressure field for the fitted and unfitted case are shown in Figs. 7(a), 7(b) and Figs. 8(a), 8(b), respectively.

6.1.1. Grid convergence

The rates of convergence were computed for the velocities and pressure separately in the usual L_2-norm by applying five regular grid refinements and comparing the solution computed on each grid with the solution on the next finer grid. To avoid imparing the convergence results by non-linear effects, the computations were additionally performed for the linear Stokes equations and identical fluid parameters. The results of the convergence rates for the linear and non-linear test cases are summarized in the Tables 1 and 2. In the linear case the rates on the boundary fitted mesh show order two for the velocity and order one for the pressure. This is in accordance with the investigations carried out in [24] for the stabilized finite volume scheme applied here. As to be expected for an unfitted scheme, Table 1 shows reduced convergence rates around 1.5 for the velocity in the linear case. In the non-linear case, the fitted and non-fitted computations show an irregular behavior. This can be traced back to the applied skewed upwind scheme for the convective terms. The rates for the pressure are irregular already for the linear case. A possible reason for that can be the changing representation of the discrete interface ∂P_h on the different grid refinements: the quality of the approximation of the interface is not necessarily improved on the next finer grid, as explained above.
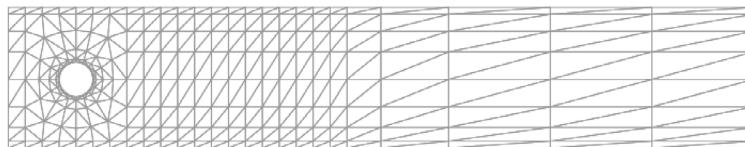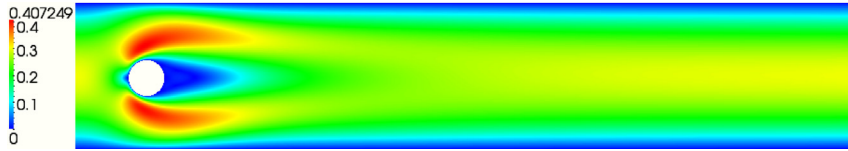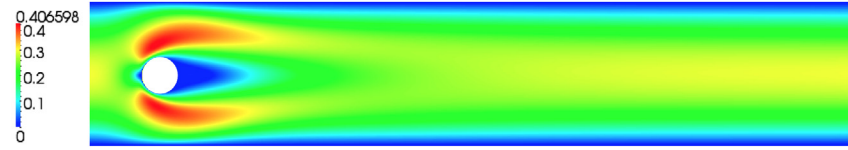

(a) boundary fitted mesh
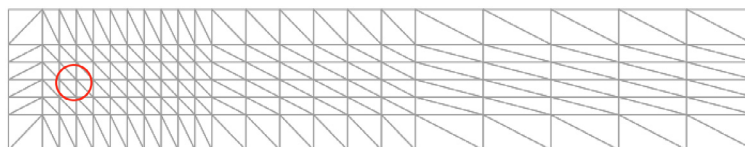
(b) unfitted mesh and immersed interface ∂P (red)

Fig. 6. Flow around a fixed cylinder: (a) boundary fitted mesh; (b) unfitted mesh.

(a) Magnitude of the velocity (color) for the boundary fitted mesh in Fig. 6a.

(b) Magnitude of the velocity (color) for the unfitted mesh in Fig. 6b.

Fig. 7. Magnitude of the velocity (color): (a) boundary fitted mesh; (b) unfitted mesh.

(a) Pressure (color) for the boundary fitted mesh in Fig. 6a.

(b) Pressure (color) for the unfitted mesh in Fig. 6b.

Fig. 8. Pressure (color): (a) boundary fitted mesh; (b) unfitted mesh.

Table 1
Grid convergence for the linear flow problem around a fixed cylinder: (a) boundary fitted mesh; (b) unfitted mesh.

l	n	h_l	$\|u\|_2$	r_l	$\|v\|_2$	r_l	$\|p\|_2$	r_l
Convergence rates for the boundary fitted mesh in Fig. 6(a)								
1	3,222	1.55e-01	5.36e-03	—	1.13e-03	—	6.88e-04	—
2	12,396	7.76e-02	1.40e-03	1.933	3.03e-04	1.899	2.50e-04	1.460
3	48,600	3.88e-02	3.56e-04	1.978	7.83e-05	1.952	9.77e-05	1.355
4	192,432	1.94e-02	8.95e-05	1.992	1.99e-05	1.977	4.14e-05	1.240
5	765,792	9.70e-03	2.24e-05	1.997	5.01e-06	1.989	1.91e-05	1.118
6	3,055,296	4.85e-03	—	—	—	—	—	—
Convergence rates for the unfitted mesh in Fig. 6(b)								
1	1,755	1.12e-01	1.06e-02	—	5.43e-03	—	1.42e-03	—
2	6,675	5.62e-02	3.62e-03	1.545	1.97e-03	1.436	5.55e-04	1.355
3	26,019	2.81e-02	1.49e-03	1.281	7.99e-04	1.306	2.70e-04	1.037
4	102,723	1.40e-02	5.75e-04	1.375	3.27e-04	1.290	1.11e-04	1.288
5	408,195	7.02e-03	2.51e-04	1.193	1.35e-04	1.272	5.60e-05	0.982
6	1,627,395	3.51e-03	—	—	—	—	—	—

6.1.2. Oscillation of the pressure

The limited approximation properties of the discrete interface were described and investigated in detail in Section 5.2. Fig. 9 shows plots of the values of the pressure along the interface. The oscillations result from bad approximation of the local gradients of the pressure along the interface. Moreover, they do not vanish under grid refinement but their frequency even increases. This observation confirms the assumption that the numerical artifact of an oscillating pressure has a local origin on each grid element and will similarly re-appear on each grid size.

Table 2
Grid convergence for the non-linear flow problem around a fixed cylinder: (a) boundary fitted mesh; (b) unfitted mesh.

l	n	h_l	$\|u\|_2$	r_l	$\|v\|_2$	r_l	$\|p\|_2$	r_l
Convergence rates for the boundary fitted mesh in Fig. 6(a)								
1	3,222	1.55e-01	2.15e-03	—	6.85e-04	—	3.90e-04	—
2	12,396	7.76e-02	6.57e-04	1.713	2.00e-04	1.776	1.67e-04	1.228
3	48,600	3.88e-02	2.07e-04	1.663	7.98e-05	1.362	1.10e-04	0.605
4	192,432	1.94e-02	6.38e-05	1.702	3.51e-05	1.184	5.41e-05	1.019
5	765,792	9.70e-03	1.85e-05	1.782	1.28e-05	1.462	2.25e-05	1.264
6	3,055,296	4.85e-03	—	—	—	—	—	—
Convergence rates for the unfitted mesh in Fig. 6(b)								
1	1,755	1.12e-01	1.40e-02	—	6.66e-03	—	2.85e-03	—
2	6,675	5.62e-02	4.18e-03	1.741	3.29e-03	1.019	1.39e-03	1.032
3	26,019	2.81e-02	1.59e-03	1.395	1.29e-03	1.347	5.12e-04	1.443
4	102,723	1.40e-02	6.34e-04	1.326	5.42e-04	1.254	2.06e-04	1.311
5	408,195	7.02e-03	2.88e-04	1.136	2.16e-04	1.330	8.45e-05	1.287
6	1,627,395	3.51e-03	—	—	—	—	—	—

Table 3
Pressure difference Δp, see (63); reference values, cf. [19].

l	Δp fitted	Δp unfitted
1	1.171767e-01	7.164115e-02
2	1.170200e-01	1.015976e-01
3	1.172432e-01	1.087336e-01
4	1.173491e-01	1.123866e-01
5	1.174222e-01	1.144121e-01
6	1.174703e-01	1.157436e-01
Reference	1.1752e-01	

(a) gird level $l = 4$ (b) grid level $l = 5$ (c) grid level $l = 6$
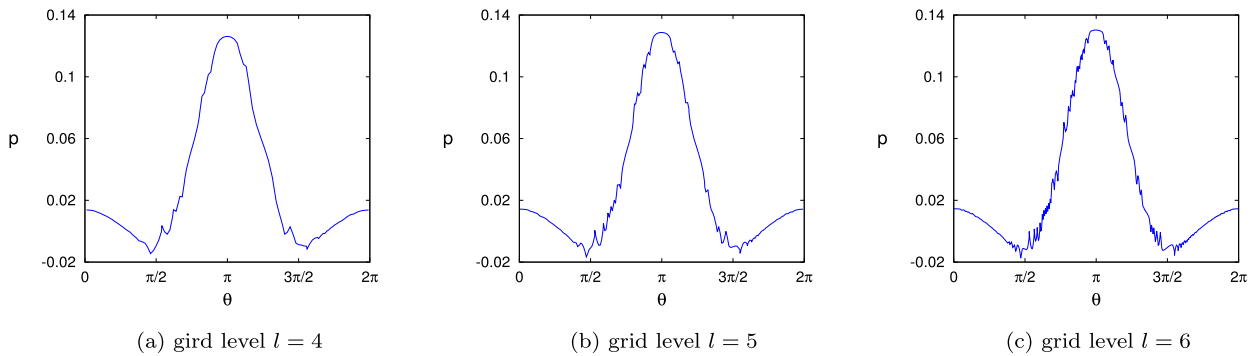
Fig. 9. Pressure along the interface $\gamma(\theta) := 0.05\,(\cos(\theta), \sin(\theta))^T$ for different grid refinements.

In order to investigate the global quality of the pressure solution, the difference

$$\Delta p(x, y) := p(0.15, 0.2) - p(0.25, 0.2) \tag{63}$$

between the front and back point of the interface was additionally evaluated. A comparison with the reference [19] is shown in Table 3.

6.2. Sedimenting particle – stationary benchmark

For the validation of the translational component $\mathbf{U}$ of a particle with radius r we conduct the test problem of a sedimenting particle falling (infinitely long) under gravity in a channel of width D, see Fig. 10. The computed stationary (long term) solution is the terminal velocity $\mathbf{U}(r) = (0, U_{\text{term}}(r))^T$ of the particle in its equilibrium between friction and gravitational acceleration. Because of the finite width D of the channel an additional so called *wall-force* F_w acts on the particle. Since F_w depends on the relation $\frac{2r}{D}$ (*blockage ratio*) the terminal velocity $U_{\text{term}}(r)$ will depend on r and D as well. There exist different asymptotic solutions for the wall force F_w in the literature. For the case of a two dimensional channel we choose

$$F_w(2r, D) := \ln\left(\frac{D}{2r}\right) - 0.9157 + 1.7244\left(\frac{2r}{D}\right)^2 - 1.7302\left(\frac{2r}{D}\right)^4 + O\left(\left(\frac{2r}{D}\right)^6\right)$$
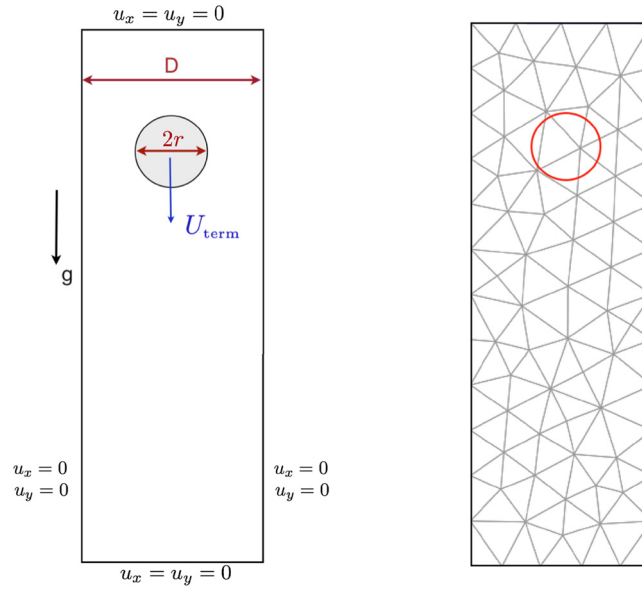
Fig. 10. Sedimenting particle: configuration of the problem (left) and unstructured mesh with immersed interface in red (right).

(a) $|\mathbf{u}_x(\vec{x})|$ (b) $|\mathbf{u}_y(\vec{x})|$ (c) $p(\vec{x})$
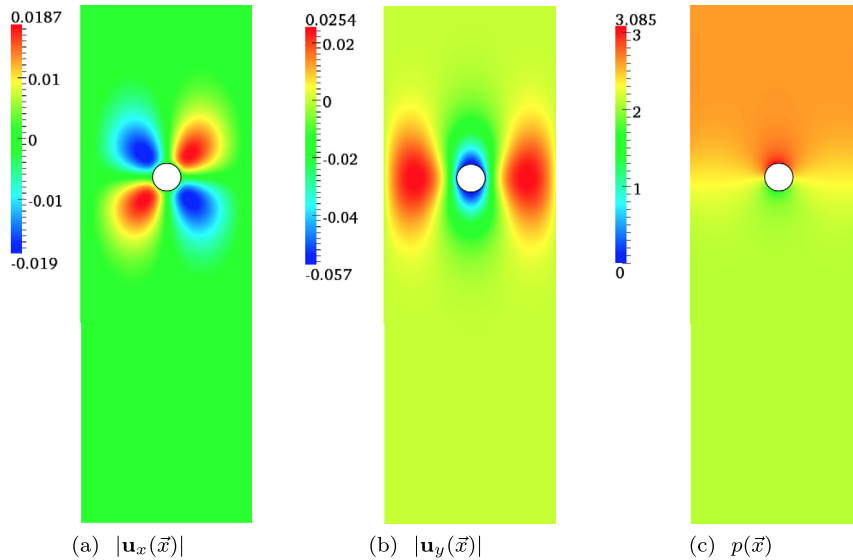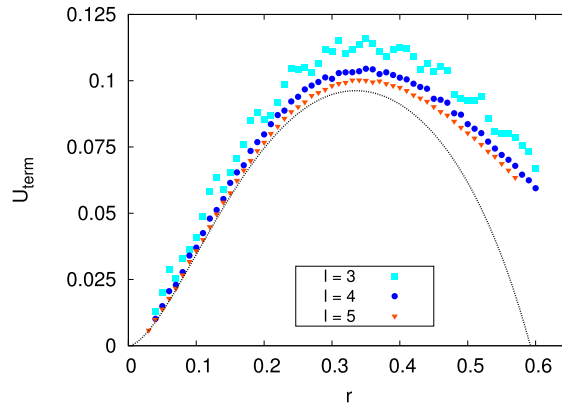
Fig. 11. Solution for the sedimenting particle (stationary benchmark) with radius $r = 0.15$ and grid level $l = 5$: (a), (b) velocity field; (c) pressure.

$$U_{\text{term}}(r) := \frac{(\rho_P - \rho_f)\, g\, r^2}{4\mu}\, F_{\text{w}}(2r, D) \tag{64}$$

as asymptotic solution, cf. [46], with gravitational acceleration g, density of the particle, ρ_P, and the density and viscosity of the fluid, ρ_f and μ. For fixed channel width the validated value $U_{\text{term}}(r)$ depends on the radius only.

The numerical tests were conducted on the unstructured mesh as shown in Fig. 10 with dimensions $\Omega = [0, 2] \times [0, 6]$. Simple no-slip Dirichlet conditions on the outer boundary are applied. Fig. 11 shows the solution for $r = 0.15$ on the 5-times refined mesh comprising $190, 419$ degrees of freedom. The computed terminal velocity is $\mathbf{U}(r) = (0, -0.0572)^T$.

For further computations the radius of the particle was varied between 0.02 and 0.55. The results for different levels of refinement are plotted in Fig. 12. For radii ≤ 0.3 the computed solutions converge nicely against the asymptotic solution, indicated with the black line in Fig. 12(a). Since the analytical solution is only asymptotically valid, i.e. for a sufficiently small radius, the distance between numerical and analytical solution increases for radii > 0.3. The according plots for the quantities $\mathbf{U}_x(r)$ and $\omega(r)$ are depicted in Figs. 12(b) and 12(c).

(a) Falling velocity $\mathbf{U}_y(r)$; asymptotic solution $U_{\text{term}}(r)$ (black), see (64).
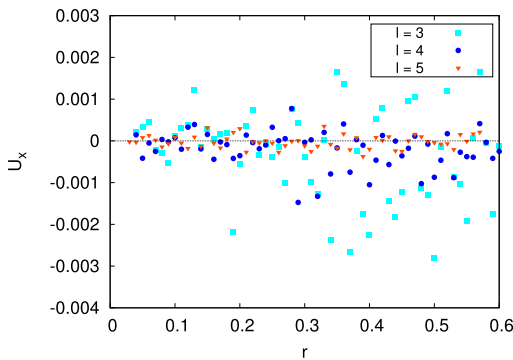
(b) Velocity $\mathbf{U}_x(r)$; analytical solution (black)
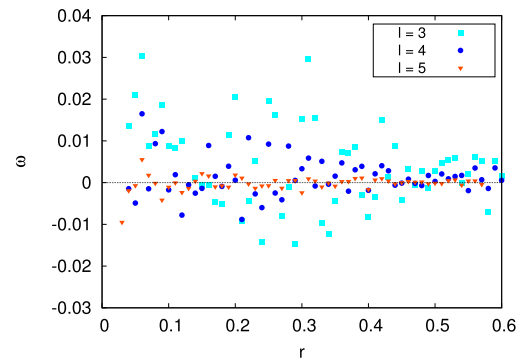
(c) Rotation $\omega(r)$; analytical solution (black)

Fig. 12. Velocity components for the sedimenting particle (stationary benchmark) for varying radius r and different levels l of grid refinement.

Table 4
l^2-error for the sedimenting particle (stationary benchmark) for $\mathbf{U}_y$, $\mathbf{U}_x$ and ω, see (65), (66).

l	n	l^2-error		
		$\epsilon_{\mathbf{U}_y}$	$\epsilon_{\mathbf{U}_x}$	ϵ_ω
3	11,607	2.762e-02	1.125e-03	1.447e-02
4	47,211	2.063e-02	4.726e-04	4.843e-03
5	190,419	1.303e-02	1.582e-04	1.866e-03

Table 4 shows the discrete l^2-norm

$$\epsilon_{\mathbf{U}_y} := \sqrt{\frac{1}{N_r} \sum_{i=1}^{N_r} [\, U_{\text{term}}(r_i) - \mathbf{U}_y(r_i)\,]^2}, \tag{65}$$

$$\epsilon_{\mathbf{U}_x} := \sqrt{\frac{1}{N_r} \sum_{i=1}^{N_r} \mathbf{U}_x(r_i)^2}, \quad \epsilon_\omega := \sqrt{\frac{1}{N_r} \sum_{i=1}^{N_r} \omega(r_i)^2}, \tag{66}$$

of the errors for all quantities $\mathbf{U}_x(r)$, $\mathbf{U}_y(r)$ and $\omega(r)$. N_r denotes the number of radii $r_i \in [0.02; 0.3]$, $i = 1, ..., N_r$, for which the test problem was computed. It is $r_{i+1} - r_i = 0.01$. Due to Corollary 3 the admissible minimal radius and along with it the number N_r differ on each grid level. Table 4 shows that the error decreases under refinement. It should be emphasized that the error is averaged over several radii. Since the quality of the approximation of the interface changes for each radius with respect to a given fixed refinement level of the grid, these measurements are not suitable to investigate the convergence properties of the scheme.

6.3. Sedimenting particle – instationary benchmarks

6.3.1. Sedimenting spherical particle

As first instationary test case we chose the problem of a sedimenting particle under gravity in a two dimensional channel with dimensions $\Omega = [0, 2] \times [0, 6]$ as for the stationary case in Section 6.2. As parameter for the particle and the fluid we set $r = 0.125$, $\rho_P = 1.25$, $\rho_f = 1.0$ and $\mu = 0.1$. No-slip Dirichlet conditions are applied on the outer boundary and initially the particle is at rest and at position $(1, 2)$. For comparison of our results we refer to Glowinski [13]. The same test case was also studied by Wan and Turek [47], Blasco et al. [5] and Krause and Kummer [21].

The test case was computed for 4 refinement levels $l = 3, ..., 6$ of the mesh as depicted in Fig. 10. The time step was refined accordingly ranging from $\Delta t = 1 \cdot 10^{-2} s$ to $0.125 \cdot 10^{-2} s$.

Fig. 13 shows the temporal evolution of the y-component of the translational velocity and the y-coordinate of the center of mass. The dotted lines indicate the zero level and the reference value $U_{\text{term}} = 5.5392$ according to [13]. The bad approximation of the interface on the coarsest level leads to oscillations in the falling velocity $\mathbf{U}_y(t)$ and strong deviations from zero for $\mathbf{U}_x(t)$ and $\omega(t)$. Under refinement, however, the terminal velocity converges to the reference value. The exact data is summarized in Table 5 together with the Reynolds number derived from the terminal velocity. For the computation of U_{term} the values of $\mathbf{U}_y(t)$ were averaged within the time interval $[0.4, 0.6]$. The Reynolds number is also in good agreement with those computed in [13], $Re = 17.31$, in [47], $Re = 17.15$ and in [5], $Re = 17.34$.
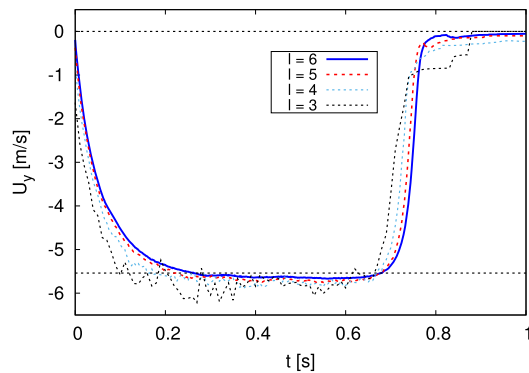
(a) Evolution of the falling velocity $\mathbf{U}_y(t)$
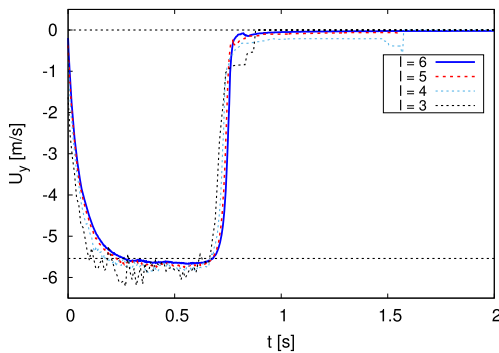
(b) Prolonged evolution of the falling velocity $\mathbf{U}_y(t)$
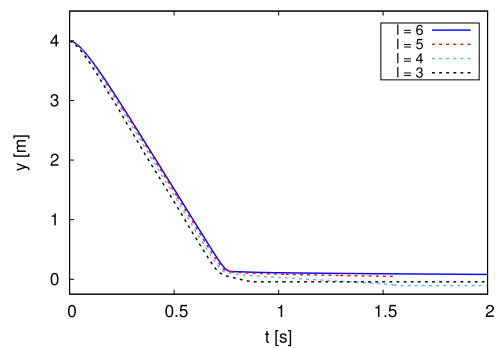
(c) Evolution of the y-coordinate of particle center

Fig. 13. Time evolution of a sedimenting particle; (b) illustrates the stable phase of the particle at rest.

Table 5
Terminal velocity and Reynolds number of a sedimenting particle and reference, cf. [13].

l	# DoFs	U_{term}	Re
3	11,607	5.8003	18.13
4	47,211	5.7656	18.02
5	190,419	5.7101	17.84
6	771,171	5.6420	17.63
Reference		5.5392	17.31

l	# DoFs	$\epsilon_{\mathbf{U}_x}$	ϵ_ω
3	11,607	0.2441	4.1670
4	47,211	0.0774	1.5782
5	190,419	0.0401	0.6903
6	771,171	0.0124	0.2603

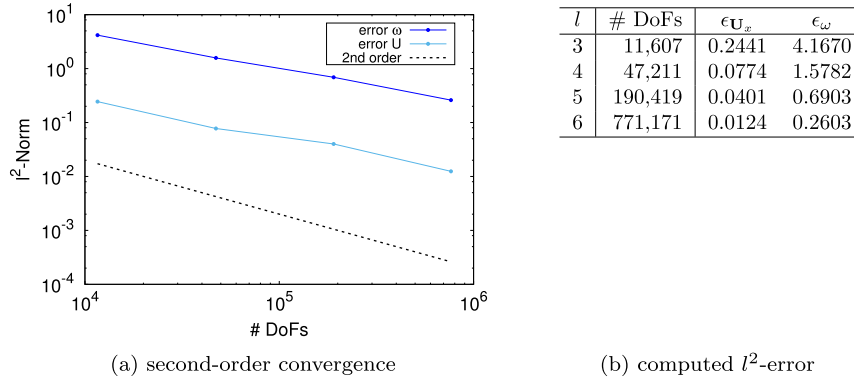(a) second-order convergence   (b) computed l^2-error

Fig. 14. l^2-error for the sedimenting particle (instat.) for $\mathbf{U}_x(t)$ and $\omega(t)$, see (67).

It should be emphasized that not only the terminal velocity itself but also the whole time evolution of the falling velocity is in good agreement with those computed by Wan and Turek [47] and Blasco et al. [5]. The important features of a fast accelerating and decelerating phase are captured well by our fully-coupled scheme. In particular, the fast deceleration runs without overshoot across the ground. That can be attributed to an efficient coupling between the particle degrees of freedom and those at the outer boundary. Of course a suitable size of the time step is necessary. However, we want to recall that no additional repellent forces were applied to avoid a collision of the immersed boundary with the ground. Many discrete schemes implement a collision force commonly depending on the distance to the wall, cf. [15], [47], [42], [44], [2], [5], [50]. Using our scheme, the simulation reaches a stable equilibrium in which the particle does not move anymore.

A further quality of our scheme is its conservation property: In the ideal case, the particle falls with constant velocity as soon as it reaches the equilibrium between gravitational acceleration and friction. Our scheme is able to reproduce that since for $t \in [0.4, 0.6]$ the simulation on the finest grid (blue line in Fig. 13(a)) follows in good approximation a horizontal line. We emphasize that on the coarser grids the influence of the grid size on the approximation is clearly visible. The horizontal course can be attributed to the fully coupled linear system of particle and fluid getting solved in one single step without application of a time splitting scheme. As an important consequence, the interaction forces are instantaneously exchanged without loss of momentum.

Finally, we studied the convergence of our scheme. For this purpose, we evaluated the l^2-error

$$\epsilon_{\mathbf{U}_x} := \sqrt{\frac{1}{N_t} \sum_{i=1}^{N_t} \mathbf{U}_x(t_i)^2}, \quad \epsilon_\omega := \sqrt{\frac{1}{N_t} \sum_{i=1}^{N_t} \omega(t_i)^2} \tag{67}$$

for the horizontal and rotational velocity whose analytical solution is zero. We considered the period of $T = 2s$ and therefore $N_t := T/\Delta t$ denotes the number of time steps taken into account for the averaging. It is $t_{i+1} = t_i + \Delta t$. The results are summarized in Fig. 14. Due to a sufficiently small time step we can observe a rate near to second order.

6.3.2. Sedimenting elliptical particle

As second instationary test case we chose the problem of a sedimenting particle with elliptical shape. The problem settings differ only slightly from the one in Subsection 6.3.1: The geometry of the channel has double length, i.e. $\Omega = [0, 2] \times [0, 12]$, in order to observe the oscillating rotation of the ellipse. Furthermore, the shape of the particle is changed to an ellipse with vertical axis 0.25 and horizontal axis 0.125. Therefore, in the initial state the long side of the ellipse points in the direction of gravity. All remaining parameter are unchanged.

The test case was computed for 3 refinement levels and accordingly refined time steps ranging from $\Delta t = 1 \cdot 10^{-2}s$ to $0.25 \cdot 10^{-2}s$.

Fig. 15 shows the temporal evolution of selected parameters of the elliptical particle. As for the spherical test Case 6.3.1, the bad approximation of the interface on the coarsest level leads to small zig-zag behavior. Under refinement, however, this artifact is smoothed out.

We want to emphasize that all parameters follow an oscillating behavior induced by the rotation of the ellipse. In particular, we can observe a certain time lag between the evolution of the rotational velocity ω (see Fig. 15(a)) and the orientation of the ellipse θ (see Fig. 15(c)), as to be expected. Furthermore, the oscillations get damped and vary around 90 degrees. So in average, the ellipse turns its broadside to the stream. Fig. 16 shows snapshots of the global magnitude of the velocity. The dynamics are in good accordance with the simulations conducted by [26]. Even though in [26] simulations are conducted in 3 spatial dimensions, the mentioned features of the motion are expected to similarly arise in 2 spatial dimensions.
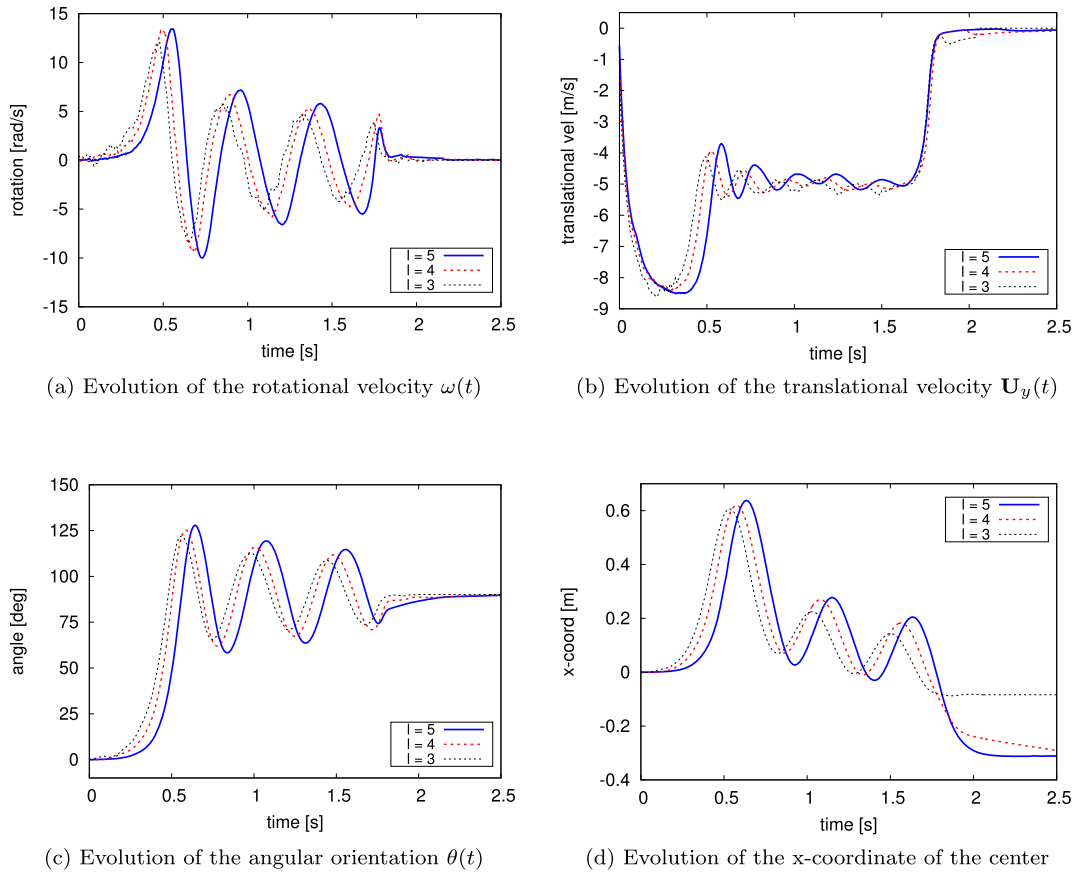
(a) Evolution of the rotational velocity $\omega(t)$

(b) Evolution of the translational velocity $\mathbf{U}_y(t)$

(c) Evolution of the angular orientation $\theta(t)$

(d) Evolution of the x-coordinate of the center

Fig. 15. Time evolution of selected parameters of a sedimenting elliptical particle.

7. Conclusions

The derivation of the described numerical scheme for particulate flow is crucially based on the employment of a finite volume scheme and its formulation as Petrov-Galerkin bilinear form. Since the operator of a finite element scheme comprises the computation of the stresses within a volume, the relevant forces cancel in the continuous formulation, see (35). The boundary integrals in (34) turned out to be more suitable, which is in agreement with the fact that the interaction takes place on the interface. Conversely, we take advantage of the usual approach within finite element methods to symmetrically extend the ansatz and test spaces. Moreover, the identification of a FV scheme with an according FE scheme enabled theoretical analysis and finally the derivation of an equivalent FEM for particulate flow.

Within the discrete finite element scheme for particulate flow the computed forces in the particle arise in the form of a thick interface on the cut elements (56). In order to estimate the error at the discrete interface the identification with the according finite volume solution reveals the real shape of the interface, cf. Fig. 4. This association enables to estimate the error at the interface by means of the deviation of the discrete gradients in normal direction to the interface. Finally, we could trace back the observed pressure oscillations to the bad approximation of the local pressure gradient.

In summary, a finite volume formulation can on the one hand facilitate the formulation of given boundary forces. On the other hand, finite element theory provides tools for the construction of mathematically favorable schemes. The modeling of particulate flow demonstrated that previous to applying a certain discretization scheme the crucial challenges and building blocks need to be figured out. Depending on the particular application either one or another scheme can be more suitable.

The derived scheme is still lacking good approximation properties for the pressure. Moreover, in multiphase flow applications where the deformation of the interface highly depends on pressure forces the pressure becomes an even more important quantity. Therefore, we want to improve the discretization by developing a sharp-interface approach. The extended spaces need to be adapted in order to obtain a sharp representation of the interface. In a forthcoming paper a second order immersed boundary finite element scheme is derived. Once again we will essentially take advantage of the identification with the finite volume method in order to choose the finite element spaces properly.
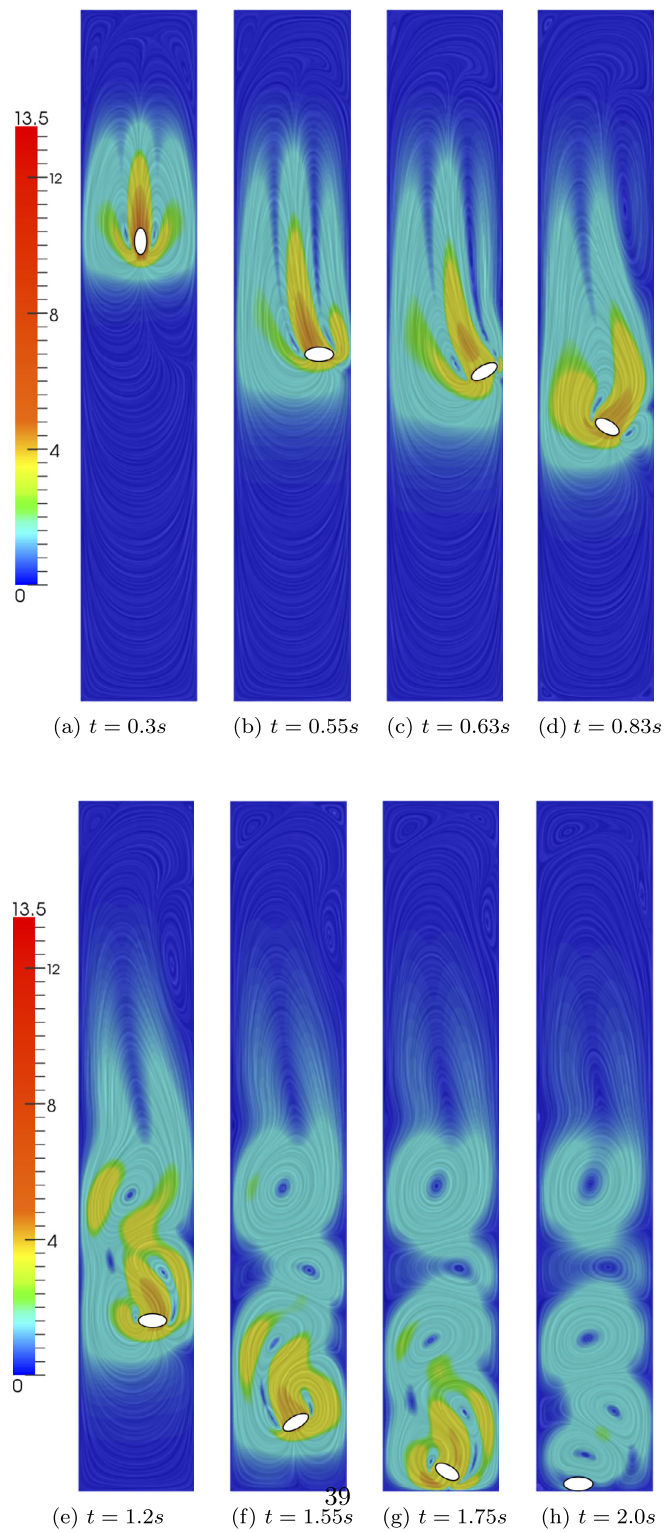
(a) $t = 0.3s$ (b) $t = 0.55s$ (c) $t = 0.63s$ (d) $t = 0.83s$

(e) $t = 1.2s$ (f) $t = 1.55s$ (g) $t = 1.75s$ (h) $t = 2.0s$

Fig. 16. Sedimenting particle: Magnitude of the velocity (color) and streamlines for different times computed on level $l = 5$.

Acknowledgements

References

[1] D.M. Anderson, G.B. McFadden, A.A. Wheeler, Diffuse-Interface methods in fluid mechanics, Annu. Rev. Fluid Mech. 30 (1) (1998) 139–165.
[2] S.V. Apte, M. Martin, N.A. Patankar, A numerical method for fully resolved simulation (FRS) of rigid particle-flow interactions in complex flows, J. Comput. Phys. 228 (8) (2009) 2712–2738.
[3] R.E. Bank, D.J. Rose, Some error estimates for the box method, SIAM J. Numer. Anal. 24 (1987) 777–787.
[4] J. Bey, Finite-Volumen- und Mehrgitterverfahren für elliptische Randwertprobleme, Dissertation, Universität, Tübingen, 1997.
[5] J. Blasco, M.C. Calzada, M. Marín, A fictitious domain, parallel numerical method for rigid particulate flows, J. Comput. Phys. 228 (20) (2009) 7596–7613.
[6] W.-P. Breugem, A second-order accurate immersed boundary method for fully resolved simulations of particle-laden flows, J. Comput. Phys. 231 (13) (2012) 4469–4498.
[7] E. Burman, M.A. Fernandez, Stabilization of explicit coupling in fluid-structure interaction involving fluid incompressibility, Comput. Methods Appl. Mech. Eng. 198 (5–8) (2009) 766–784.
[8] L. Chen, Fitine volume methods, Private communication, http://www.math.uci.edu/~chenlong/226/FVM.pdf, 2010.
[9] C.M. Elliott, B. Stinner, V. Styles, R. Welford, Numerical computation of advection and diffusion on evolving diffuse interfaces, IMA J. Numer. Anal. 31 (2011) 786–812.
[10] E.A. Fadlun, R. Verzicco, P. Orlandi, J. Mohd-Yusof, Combined immersed-boundary finite-difference methods for three-dimensional complex flow simulations, J. Comput. Phys. 161 (1) (2000) 35–60.
[11] J. Feng, H.H. Hu, D.D. Joseph, Direct simulation of initial value problems for the motion of solid bodies in a Newtonian fluid, part 1: sedimentation, J. Fluid Mech. 261 (1994) 95–134.
[12] J. Feng, H.H. Hu, D.D. Joseph, Direct simulation of initial value problems for the motion of solid bodies in a Newtonian fluid, part 2: Couette and Poiseuille flows, J. Fluid Mech. 277 (1994) 271–301.
[13] R. Glowinski, Finite element methods for incompressible viscous flow, in: P.G. Ciarlet, J.L. Lions (Eds.), Handbook of Numerical Analysis IX, North-Holland, Amsterdam, 2003.
[14] R. Glowinski, T.-W. Pan, T.I. Hesla, D.D. Joseph, A distributed Lagrange multiplier/fictitious domain method for particulate flows, Int. J. Multiph. Flow 25 (1999) 755–794.
[15] R. Glowinski, T.-W. Pan, T.I. Hesla, D.D. Joseph, J. Périaux, A fictitious domain approach to the direct numerical simulation of incompressible viscous flow past moving rigid bodies: application to particulate flow, J. Comput. Phys. 169 (2) (2001) 363–426.
[16] M.D. Griffith, J.S. Leontini, Sharp interface immersed boundary methods and their application to vortex-induced vibration of a cylinder, J. Fluids Struct. 72 (2017) 38–58.
[17] W. Hackbusch, On First and Second Order Box Schemes, Computing 41 (4) (1989) 277–296.
[18] H.H. Hu, N.A. Patankar, M.Y. Zhu, Direct numerical simulations of fluid-solid systems using the arbitrary Lagrangian-Eulerian technique, J. Comput. Phys. 169 (2001) 427–462.
[19] V. John, G. Matthies, Higher-order finite element discretizations in a benchmark problem for incompressible flows, Int. J. Numer. Methods Fluids 37 (2001) 885–903.
[20] A.A. Johnson, T.E. Tezduyar, Simulation of multiple spheres falling in a liquid-filled tube, Comput. Methods Appl. Mech. Eng. 134 (3–4) (1996) 351–373.
[21] D. Krause, F. Kummer, An incompressible immersed boundary solver for moving body flows using a cut cell discontinuous Galerkin method, Comput. Fluids 153 (2017) 118–129.
[22] J.E. Marsden, T.J.R. Hughes, Mathematical foundations of elasticity, SIAM J. Numer. Anal. (1983).
[23] R. Mittal, G. Iaccarino, Immersed boundary methods, Annu. Rev. Fluid Mech. 37 (1) (2005) 239–261.
[24] S. Nägele, Mehrgitterverfahren für die inkompressiblen Navier-Stokes Gleichungen im laminaren und turbulenten Regime unter Berücksichtigung verschiedener Stabilisierungsmethoden, Dissertation, Universität Heidelberg, 2003.
[25] S. Nägele, G. Wittum, On the influence of different stabilisation methods for the incompressible Navier-Stokes equations, J. Comput. Phys. 224 (2007) 100–116.
[26] T.-W. Pan, R. Glowinsky, D.D. Joseph, R. Bai, Direct simulation of the motion of settling ellipsoids in Newtonian fluid, in: Fourteenth International Conference on Domain Decomposition Methods, 2003, pp. 119–129.
[27] N.A. Patankar, A formulation for fast computations of rigid particulate flows, Annu. Res. Briefs (2001) 185–196.
[28] N.A. Patankar, P. Singh, D.D. Joseph, R. Glowinski, T.-W. Pan, A new formulation of the distributed Lagrange multiplier/fictitious domain method for particulate flows, Int. J. Multiph. Flow 26 (9) (2000) 1509–1524.
[29] C.S. Peskin, Numerical analysis of blood flow in the heart, J. Comput. Phys. 25 (1977) 220–252.
[30] C.S. Peskin, The immersed boundary method, Acta Numer. 11 (2002) 479–517.
[31] R. Prignitz, E. Bänsch, Particulate flows with the subspace projection method, J. Comput. Phys. 260 (2014) 249–272.
[32] H. Reichert, G. Wittum, Solving the Navier-Stokes equations on unstructured grids, in: Flow Simulation with High-Performance Computers I, 1993, p. 38.
[33] S. Reuther, A. Voigt, Incompressible two-phase flows with an inextensible Newtonian fluid interface, J. Comput. Phys. 322 (2016) 850–858.
[34] M. Schäfer, S. Turek, Benchmark computations of laminar flow around a cylinder, in: Flow Simulation with High-Performance Computers II, in: Notes on Numerical Fluid Mechanics, vol. 2, 1996, pp. 547–566.
[35] N. Sharma, N.A. Patankar, A fast computation technique for the direct numerical simulation of rigid particulate flows, J. Comput. Phys. 205 (2) (2005) 439–457.
[36] K.E. Teigen, X. Li, J. Lowengrub, F. Wang, A. Voigt, A diffuse-interface approach for modeling transport, diffusion and adsorption/desorption of material quantities on a deformable interface, Commun. Math. Sci. 4 (7) (2009) 1009–1037.
[37] K.E. Teigen, P. Song, J. Lowengrub, A. Voigt, A diffuse-interface method for two-phase flows with soluble surfactants, J. Comput. Phys. 230 (2) (2011) 375–393.
[38] S. Tschisgale, T. Kempe, J. Fröhlich, A non-iterative immersed boundary method for spherical particles of arbitrary density ratio, J. Comput. Phys. 339 (2017) 432–452.
[39] M. Uhlmann, An immersed boundary method with direct forcing for the simulation of particulate flows, J. Comput. Phys. 209 (2) (2005) 448–476.
[40] M. Uhlmann, J. Dušek, The motion of a single heavy sphere in ambient fluid: A benchmark for interface-resolved particulate flow simulations with significant relative velocities, Int. J. Multiph. Flow 59 (2014) 221–243.
[41] S.O. Unverdi, G. Tryggvason, A front-tracking method for viscous, incompressible, multi-fluid flows, J. Comput. Fluids 100 (1992) 25–37.

[42] C. Veeramani, P.D. Minev, K. Nandakumar, A fictitious domain formulation for flows with rigid particles: A non-Lagrange multiplier version, J. Comput. Phys. 224 (2) (2007) 867–879.
[43] A. Vogel, S. Reiter, M. Rupp, A. Nägel, G. Wittum, UG 4: A novel flexible software system for simulating PDE based models on high performance computers, Comput. Vis. Sci. 16 (2013) 165–179.
[44] A. Wachs, A DEM-DLM/FD method for direct numerical simulation of particulate flows: Sedimentation of polygonal isometric particles in a Newtonian fluid with collisions, Comput. Fluids 38 (8) (2009) 1608–1628.
[45] A. Wachs, A. Hammouti, G. Vinay, M. Rahmani, Accuracy of finite volume/staggered grid distributed Lagrange multiplier/fictitious domain simulations of particulate flows, Comput. Fluids 115 (2015) 154–172.
[46] G.J. Wagner, N. Moës, W.K. Liu, T. Belytschko, The extended finite element method for rigid particles in Stokes flow, Int. J. Numer. Methods Eng. 51 (2001) 293–313.
[47] D. Wan, S. Turek, Direct numerical simulation of particulate flow via multigrid FEM techniques and the fictitious boundary method, Int. J. Numer. Methods Fluids 51 (5) (2006) 531–566.
[48] D. Wan, S. Turek, Fictitious boundary and moving mesh methods for the numerical simulation of rigid particulate flows, J. Comput. Phys. 222 (1) (2007) 28–56.
[49] J. Xu, Q. Zou, Analysis of linear and quadratic simplicial finite volume methods for elliptic equations, Numer. Math. 111 (3) (2009) 469–492.
[50] J. Yang, F. Stern, A non-iterative direct forcing immersed boundary method for strongly-coupled fluid-solid interactions, J. Comput. Phys. 295 (2015) 779–804.
[51] X. Ye, On the relationship between finite volume and finite element methods applied to the Stokes equations, Numer. Methods Partial Differ. Equ. 17 (2001) 440–453.
[52] Z. Yu, X. Shao, A direct-forcing fictitious domain method for particulate flows, J. Comput. Phys. 227 (1) (2007) 292–314.